Noise and Bandwidth of Current Recordings from Submicrometer Pores and Nanopores

Jeffrey D. Uram,[†] Kevin Ke,[†] and Michael Mayer[†,‡,*]

[†]Department of Biomedical Engineering and [‡]Department of Chemical Engineering, University of Michigan, Ann Arbor, Michigan 48109

ABSTRACT Nanopores and submicrometer pores have recently been explored for applications ranging from detection of single molecules, assemblies of nanoparticles, nucleic acids, occurrence of chemical reactions, and unfolding of proteins. Most of these applications rely on monitoring electrical current through these pores, hence the noise and signal bandwidth of these current recordings are critical for achieving accurate and sensitive measurements. In this report, we present a detailed theoretical and experimental study on the noise and signal bandwidth of current recordings from glass and polyethylene terephthalate (PET) membranes that contain a single submicrometer pore or nanopore. We examined the theoretical signal bandwidth of two different pore geometries, and we measured the signal bandwidth of the electronics used to record the ionic current. We also investigated the theoretical noise generated by the substrate material, the pore, and the electronics used to record the current. Employing a combination of theory and experimental results, we were able to predict the noise in current traces recorded from glass and PET pores with no applied voltage with an error of less than 12% in a range of signal bandwidths from 1 to 40 kHz. In approximately half of all experiments, application of a voltage did not significantly increase the noise. In the other half of experiments, however, application of a voltage resulted in an additional source of noise. For these pores, predictions of the noise were usually still accurate within 35% error at signal bandwidths of at least 10 kHz. The power spectra of this extra noise suggested a $1/f^{\alpha}$ origin with best fits to the power spectrum for $\alpha = 0.4-0.8$. This work provides the theoretical background and experimental data for understanding the bandwidth requirements and the main sources of noise in current recordings; it will be useful for minimizing noise and achieving accurate recordings.

KEYWORDS: nanopores · submicrometer pores · signal bandwidth · noise bandwidth · current recording · resistive-pulse sensing · Coulter counter

Membranes that contain a single submicrometer pore or nanopore are attracting rapidly increasing interest from a broad community of scientists in nanotechnology, chemistry, physics, engineering, and the life sciences.[1–9] This interest partially stems from the ability of these pores to act as a sensitive transducer that can detect nanoparticles, individual macromolecules, and even individual small molecules in solution.[1–6] In these experiments, a voltage is applied across the membrane and the ionic current flowing through the pore is monitored. Two parameters of critical importance for pore-based sensing are the signal bandwidth and the current noise.[10–13] The signal bandwidth determines the accuracy with which a temporal change in the current flowing through the pore is detected while the noise directly influences the sensitivity of a given pore. Here we present a detailed theoretical and experimental study on the signal bandwidth and the noise of current recordings from synthetic membranes that contain a single submicrometer pore or nanopore with the goal of enabling optimization and accurate prediction of these two parameters as well as providing guidelines for achieving reliable and sensitive low-noise recordings from these pores.

Recent advances in fabricating membranes that contain a single submicrometer pore or nanopore[7,14–46] have generated a dramatic increase in the number of applications that use these pores for sensing.[7,14,15,17,19,22–27,32,37,44,47–122] The largest body of work has been generated by using these pores for resistive-pulse sensing experiments. These experiments monitor the transient change in current (resistive-pulse) when an object of interest passes through the pore. Resistive-pulse sensing has been used to detect and characterize: (i) synthetic polymers,[70,71] (ii) DNA and RNA,[14,19,24–26,32,37,68,69,72,83–110,119,120] (iii) nanoparticles,[17,22,27,44,73–77,111] (iv) viruses[80–82] and antibody-virus interactions,[49] (v) proteins[23,27,49,58,59,112,117,123–125] and unfolding of proteins,[121] (vi) small molecules,[15,26,113–116,118] (vii) ligand binding,[60] (viii) chemical reactions,[7,56,57,64,65] and (ix) the aggregation of nanoparticles (diameter > 235 nm) by cross-linking with antibodies.[47,48,78,79] Additional work using current recordings from synthetic membranes with a single nanopore has

*Address correspondence to mimayer@umich.edu.

Received for review October 25, 2007 and accepted March 31, 2008.

Published online April 24, 2008.
10.1021/nn700322m CCC: $40.75

included studies on the fundamental aspects of ion transport through the pore,[50–54,66,67] on the tomography of a laser focus, [61] and on the effect of surface properties of the pore on the generation of 1/*f* noise.[55,62,63]

The signal bandwidth and the noise of the current recordings are important parameters for almost all of these applications. For quantitative resistive-pulse sensing experiments (*i.e.*, experiments that make use of the peak amplitudes or widths of resistive-pulses), the signal bandwidth must be sufficient to resolve fully the resistive-pulses[12,27,126] otherwise the data may be inaccurate. Ensuring a high signal bandwidth increases the information content and accuracy of the recordings. High signal bandwidth, however, also strongly increases the noise of the current recordings; this noise limits the signal-to-noise ratio and hence the sensitivity of the pore because the amplitude of a resistive-pulse must be above the noise to be detectable.[44,63] By determining the individual sources of noise, it may be possible to design the pore and the experimental setup in a fashion that minimizes the noise, and to predict accurately the current noise of a given experiment. Accurate prediction of noise combined with equations that predict the peak amplitude of a resistive-pulse[17,22,73,74,84,89,127,128] may enable the simulation of resistive-pulse sensing experiments and aid in experiment design (*e.g.*, for choosing the optimal geometry and diameter of the pores for a given application or the ideal substrate material in which the pore is fabricated).

Previous studies on the signal bandwidth and the noise of current recordings have been performed in the context of patch-clamp experiments[10,11,13,129–134] and planar lipid bilayer experiments.[12,135] Several recent studies examined the noise of current recordings from nanopores fabricated in synthetic membranes[120] as well as techniques for reducing the noise of these recordings;[22,63,120] however, the underlying individual sources of noise were not examined in detail, and methods for accurately predicting the noise of the recordings were not discussed. Here, we present a detailed theoretical and experimental study on both the signal bandwidth and the noise of current recordings from synthetic membranes that contain a single submicrometer pore or nanopore. We examine the signal bandwidth of each experimental element (*i.e.*, pore, headstage-amplifier-analog filter, digitizer, and digital filter) that was used for recording, as well as the overall signal bandwidth of these recordings. We discuss the individual sources of noise that are expected to contribute to the overall noise of the recordings, and we present theoretical equations describing these noise sources. By combining theory with experiments, we were able to predict the total noise of the recorded current traces with high accuracy for pores that did not display significant extra noise (approximately half of all experiments fell in this category).

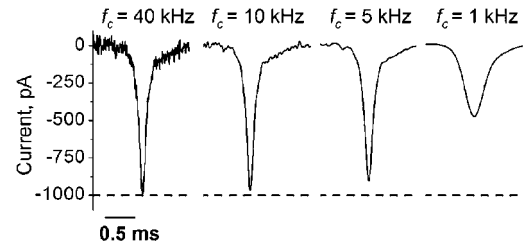

Figure 1. Comparison of a single resistive-pulse from an icosahedrical virus particle passing through a conical pore at four different signal bandwidths: 40, 10, 5, and 1 kHz. Since complete resolution of the resistive-pulse required a signal bandwidth of at least 10 kHz (see Supporting Information), [49] the shape of the resistive-pulse was modified significantly at signal bandwidths less than this value. Note: the nonrectangular shape of the resistive-pulses was not due to insufficient time resolution of the recording since the amplitude of the peaks was the same at a bandwidth of 10 and 40 kHz. Instead, this completely resolved, nonrectangular shape was a consequence of the small, spheroidal shape of the virus particles and the conical shape of the pore (which generated a short effective sensing zone).

RESULTS AND DISCUSSION

Overall Signal Bandwidth of Current Recordings from Submicrometer Pores and Nanopores. In the context of resistive-pulse sensing experiments, the signal bandwidth can limit the accuracy of measurements of peak amplitude and peak width; for example, if resolving the resistive-pulses requires a larger bandwidth than what is available, then the peak amplitude of the resistive-pulses may be "clipped" (Figure 1) or the duration of the resistive-pulse may be too short to be detected.[11,126] The overall signal bandwidth of the current recording is determined by a combination of the signal bandwidths of each individual element involved in the measurement of the ionic current. Here the individual elements are the submicrometer pore or nanopore, the headstage and amplifier, the analog low-pass filter (which prevents aliasing[11] and reduces noise), the digitizer, and, if used, the digital filter. The overall signal bandwidth will always be less than or equal to the lowest signal bandwidth available from each individual element, and determining an exact value for each element can be difficult (it is, however, possible to group certain elements and measure the signal bandwidth of this group). In general, if the signal bandwidth of an element is approximately three times greater than the lowest signal bandwidth, its contribution to the overall signal bandwidth of the recordings is negligible.[126] In the following sections, we examine the signal bandwidth of the submicrometer pore or nanopore, the headstage and amplifier, the analog filter, the digitizer, and the digital filter (or a grouping of these elements) as well the overall signal bandwidth of the current recordings.[136]

Signal Bandwidth of the Pore. Submicrometer pores and nanopores are typically fabricated in dielectric materials such as glass, silicon dioxide, silicon nitride, and polymers. The use of such materials as substrates makes it possible to model the pore as a network of resistive

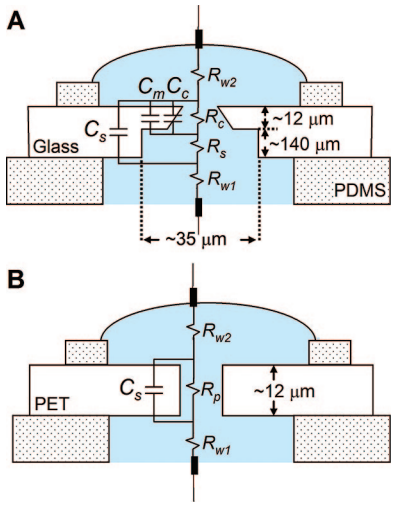

Figure 2. Simplified model circuits of the pores used in this work. (A) Model circuit of the glass pores with conical geometry. R_{w1} and R_{w2} are the resistance of the fluidic channels leading to the glass substrate, R_s is the resistance of the 35 μm wide cylindrical shank, C_s is the capacitance of the substrate supporting the glass membrane with the pore, R_c is the total resistance of the conical part of the pore structure, C_c is the total capacitance of the conical part of the pore structure, and C_m is the capacitance of the glass membrane in which the pore was fabricated. (B) Model circuit of the PET pores with cylindrical geometry. R_p is the resistance of the pore. The model circuits shown above do not include the resistance or capacitance of the electrodes since these parameters are not expected to affect significantly the signal bandwidth of the pore. In the models shown in panels A and B, we considered the convergence resistance[138,139] to and from the pore as a part of the resistance of the pore (*i.e.*, R_p and R_c include the convergence resistance).

and capacitive components.[10,13] Consequently, it is possible that the pore structure itself could limit the signal bandwidth of the measurement (the simplified circuit models we present here are intended as a tool for estimating the bandwidth of the pore and not for fitting electrochemical impedance spectra[137]).[11,13,131] In the simple case of a cylindrical pore spanning a membrane (as in the PET pores we used, see Figure 2B), the signal bandwidth of the pore can be estimated using the following equation:[13,131]

$$f_c \leq \frac{1}{2\pi RC} \quad (1)$$

where f_c (Hz) is the cutoff frequency (*i.e.*, signal bandwidth), C (F) is the capacitance of the membrane that supports the pore, and R (Ω) is the total resistance leading to and from the membrane in which the pore is fabricated. Note, in this model circuit for a pore in an electrolyte, R is *not* the resistance of the pore itself; R is only the resistance that arises in *series* with the capacitance of the chip (*i.e.*, only the resistance to and from the pore is considered in this approach).

In the experiments performed here, we used glass pores with conical geometry as shown in Figure 2A as well as polyethylene terephthalate (PET) pores with cylindrical geometry as shown in Figure 2B. For the glass pores with conical geometry, eq 1 is not directly applicable; however, it may be used to provide an estimate of the signal bandwidth for these pores by determining the lower value of the bandwidth as calculated with the following two sets of parameters (see Figure 2 for definitions of parameters): (1) $C = C_s$ and $R = R_{w1} + R_{w2}$ and (2) $C = C_m + C_c$ and $R = R_{w1} + R_{w2} + R_s$. In the fluidic setup we used with the recording buffer of lowest conductivity, R_{w1} was ~100 Ω, R_{w2} was ~1.1 kΩ, R_s was ~80 kΩ, C_s was ~10 pF, C_m was ~5 fF, and C_c was ~2 fF. Using the two parameter sets for eq 1 resulted in a signal bandwidth of ~13 MHz for parameter set 1 and ~280 MHz for parameter set 2. Taking the conservative estimate of the lower value thus predicts that we expect the signal bandwidth of the glass pores with conical geometry to be ~13 MHz.[140] For the PET pores, R_{w1} was ~20 Ω, R_{w2} was ~300 Ω, and C_s was ~30 pF. Using eq 1, these values result in an estimated signal bandwidth of 16 MHz for the PET pores. In summary, we estimate that the signal bandwidth of the pore structures we used here was in the low MHz range, which is significantly greater than the signal bandwidth of the recording electronics we used (~52 kHz, see below).[141]

Signal Bandwidth of the Headstage, Amplifier, Analog Low-Pass Filter, And Digitizer. The manufacturer of the headstage and amplifier used in this work does not specify the signal bandwidth of these individual elements. Instead, the headstage (*H*), the amplifier (*A*), and an analog low-pass Bessel filter (*F*) are grouped together and the maximum signal bandwidth of this *HAF* group is specified in the form of a no load (*i.e.*, no external components such as electrodes attached to the headstage) 10−90% risetime. The 10−90% risetime t_{10-90} (s) can be used to estimate the signal bandwidth of the *HAF* combination by using the following relationship:[126,142]

$$f_c \approx \frac{0.34}{t_{10-90}} \quad (2)$$

In the work presented here, we used two of the three amplification modes available in the Axopatch 200B amplifier: a headstage amplification of β = 0.1 and of β = 1. For β = 0.1, the feedback resistor in the headstage of the amplifier R_f equals 50 MΩ and the amplifier is able to pass a maximum current of 200 nA. For β = 1, R_f equals 500 MΩ and the amplifier is able to pass a maximum current of 20 nA.[143] The manufacturer of the amplifier specifies that the two modes of headstage amplification β = 0.1 and β = 1 have a t_{10-90} risetime of 6 μs when an analog low-pass Bessel filter with eight poles and a cutoff frequency of 100 kHz is used and no load is applied to the input. This risetime corresponds to a signal bandwidth (eq 2) of 57 kHz.[144]

Since the signal bandwidth of the *HAF* combination is a very important parameter, we also determined it experimentally.[131,145] For this measurement, we added

the digitizer (*D*) to the grouping (*HAFD*) in order to record the data. Using the built in low-pass Bessel filter with four poles set to a cutoff frequency of 100 kHz and a square wave that was capacitively coupled into the amplifier (see Experimental Section), we measured a no load t_{10-90} risetime of 6.3 ± 0.8 μs corresponding to a signal bandwidth of 54 ± 6 kHz for β = 0.1 and a t_{10-90} risetime of 6.5 ± 0.7 μs corresponding to a signal bandwidth of 52 ± 5 kHz for β = 1. When we loaded the system with a glass or a PET substrate that contained a single pore (the resistance of the pore ranged from 0.2 MΩ to 4.3 GΩ), the t_{10-90} risetime of either mode changed by less than 3.2%. In summary, the signal bandwidth of the *HAFD* combination was close to the value specified by the manufacturer for the *HAF* combination, and the signal bandwidth of the *HAFD* combination was minimally affected when loaded with electrodes and electrolyte-filled pores of either substrate material.

Overall Signal Bandwidth of Current Recordings before and after Application of a Digital Filter. Since the signal bandwidth of the pores that we used was significantly greater than the signal bandwidth of the *HAFD* combination, the overall signal bandwidth of the current recordings was set by the *HAFD* combination to ~52 kHz.[146] After recording and digitizing original current traces, it is common practice to filter these data with low-pass digital filters to reduce the noise. The effect of digital filtering on the overall signal bandwidth can be complicated to predict depending on the type of filter used and depending on the cutoff frequency of the filter compared to the overall signal bandwidth of the originally recorded current trace.[147] For all discussions in the work presented here, we experimentally determined the overall signal bandwidth of the digitally filtered current traces by measuring the t_{10-90} risetime of a digitally filtered square wave that was coupled in capacitively.[148]

Noise of Current Recordings from Submicrometer Pores and Nanopores. In this work, we characterized the current noise by two parameters: (1) the root-mean-square (rms) noise, which here is the standard deviation of the noise from its mean value, [11] and (2) the power spectral density (also known as power spectrum) of the noise. The power spectral density provides information on the distribution of the power of the noise (which can be thought of as the strength of the noise signal) as a function of frequency. This information can be useful for determining the origin of the noise.[10,11] Throughout this report, we describe the theoretical and experimental noise of the current traces based on rms values and power spectral densities. The rms noise values can be obtained easily from power spectral densities (described in the next paragraph) or from original current traces. In the following sections, we examine in detail the theoretical noise from each component involved in recording the ionic current flowing through a synthetic pore (*i.e.*, pore, headstage and amplifier, filter, *etc.*).

Theoretical Calculations of the rms Current Noise from Power Spectral Densities. Before beginning a comprehensive analysis of the noise, we will briefly discuss a detail that enables an accurate calculation of the predicted rms noise from the theoretical power spectral densities. Equations that provide rms values of the noise are derived by integrating the power spectral density of the noise with respect to frequency *f* from 0 to the cutoff frequency f_c of the filter (see eqs 3 and 4). This approach assumes that the noise from a given source is completely attenuated at frequencies above the cutoff frequency that is used in the calculation; however, the filters (digital or analog) commonly used in recording the ionic currents from the pores do not display this ideal behavior (*i.e.*, the gain of the filter is not equal to 0 above the cutoff frequency of the filter)[10] which can lead to an appreciable amount of noise power above the cutoff frequency of the filter.

This additional noise can be taken into account by using the noise bandwidth of the filter in place of the signal bandwidth in theoretical calculations of rms noise.[136] This noise bandwidth is calculated by multiplying the signal bandwidth of the filter with coefficients that are determined by the type of filter and by the frequency dependence of the power spectral density.[10] For a low-pass Bessel filter with eight poles, the correction coefficients are: $c_1 = 1.04$ for a noise source with a power spectral density that has no dependence on frequency; $c_2 = 1.3$ for a noise source with a power spectral density that grows linearly as a function of *f*; and $c_3 = 1.9$ for a noise source with a power spectral density that grows as a function of f^2.[10,149]

Theoretical Noise Generated by the Headstage and Amplifier. In nearly all current recordings from submicrometer pores or nanopores, the recording electronics convert the measured current into a voltage signal by using a current-to-voltage (*I*−*V*) converter. This *I*−*V* converter generates the majority of the noise that is added to the current signal in the headstage and amplifier.[131] The power spectral density of the noise of an *I*−*V* converter $S_A^2(f)$(A^2 Hz^{-1}) is given by eq 3 and the rms noise of an *I*−*V* converter $I_A(f_c)$ (A rms) is given by eq 4:[11]

$$S_A^2(f) = 2qI_{fet} + \frac{4akT_h}{R_f} + e_n^2\left(\frac{1}{R_f^2} + 4\pi^2 C_t^2 f^2\right) \quad (3)$$

$$I_A(f_c) = \sqrt{2qI_{fet}c_1 f_c + \frac{4akT_h c_1 f_c}{R_f} + e_n^2\left(\frac{c_1 f_c}{R_f^2} + \frac{4}{3}\pi^2 C_t^2 c_3 f_c^3\right)} \quad (4)$$

where *q* (C) is the elementary charge of an electron, 1.6 ×10^{-19} C, I_{fet} (A) is the gate leakage current of the input field effect transistor (FET), *a* (unitless) is a constant

factor that represents excess noise,[11] T_h (K) is the temperature of the feedback resistor, R_f (Ω) is the resistance of the feedback resistor, e_n (V Hz$^{-1/2}$) is the input voltage noise of the input FET of the $I-V$ converter, and C_t (F) is the total capacitance that interacts with the input of the headstage.

The first term in the power spectral density (eq 3) $2qI_{fet}$ represents the shot noise generated by the gate leakage current of the input FET of the $I-V$ converter. The input FETs used for patch-clamp amplifiers like the Axopatch 200 series are designed to exhibit low shot noise and have I_{fet} values of ~0.2 pA,[11] which is the value that we used for calculations. The second term $\{4akT/R_f\}$ represents the thermal noise generated by the feedback resistor. As stated above, the constant a is used to account for excess noise that may be present in the feedback resistor.[11] The headstage of the patch-clamp amplifier we used was cooled so that $T_h \approx 258$ K, and R_f was either 50 MΩ ($\beta = 0.1$) or 500 MΩ ($\beta = 1$). The third term $e_n^2(\{1/R_f^2\}+4\pi^2C_t^2f^2)$ represents the noise generated by the interaction of the input voltage noise with the input capacitance. The value of e_n ranges from 2−3 nV Hz$^{-1/2}$,[11] and we used a value of 3 nV Hz$^{-1/2}$ for e_n in the calculations here. The total input capacitance C_t is equal to the sum of the capacitance in the amplifier C_a and the capacitance of the dielectric material(s) C_d that interact(s) with the headstage (see preceding section for numerical values of C_d). With no load connected to the input pins, C_t is equal to C_a. For a headstage amplification of $\beta = 0.1$, the value of C_a is ~70 pF (*i.e.*, the sum of the capacitance of the FET, which is ~20 pF, and an injection capacitance of 50 pF[11]). For a headstage amplification of $\beta = 1$, C_a is ~25 pF (*i.e.*, the sum of the gate capacitance of the FET, which is ~ 20 pF, and an injection capacitance of 5 pF[11]).

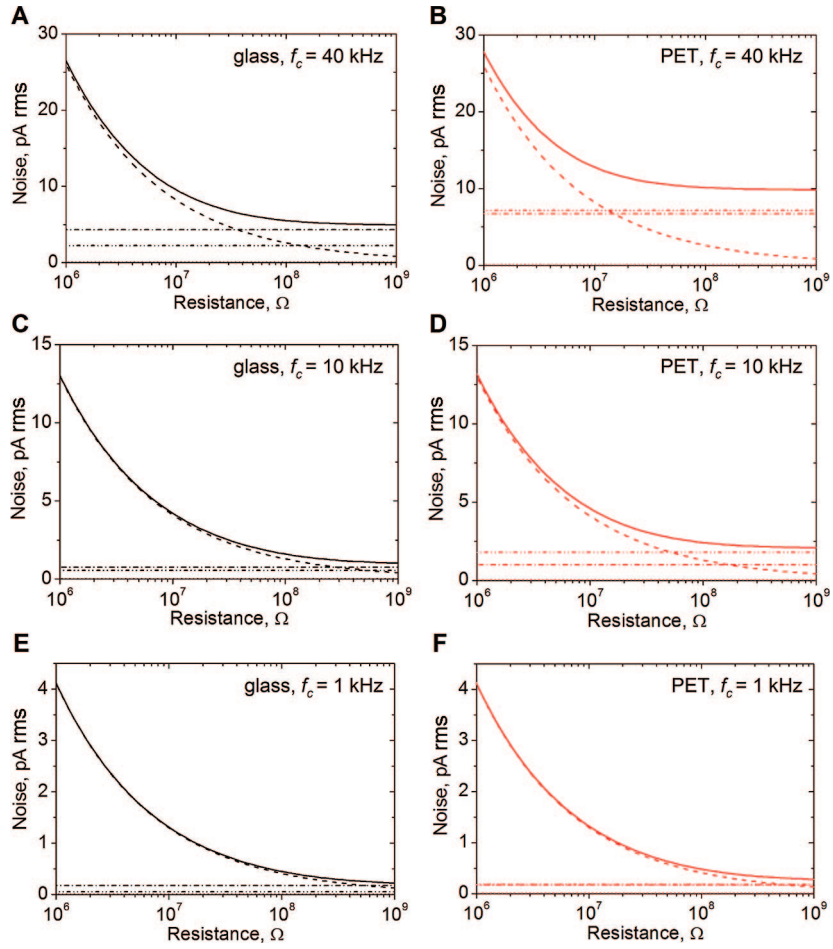

Figure 3. Magnitude of four individual theoretical noise sources and the total theoretical noise in current recordings from submicrometer pores and nanopores as a function of the resistance of the pore structure for a headstage amplification of $\beta = 1$ ($R_f = 500$ MΩ, $C_a = 25$ pF, and the overall gain of the amplifier $G = 500$ MV A^{-1}) assuming no excess noise in the feedback resistor ($a = 1$, other parameters as listed in the text). (A) Predicted noise for the glass pores used in this work at a cutoff frequency of $f_c = 40$ kHz for all sources of noise. The dashed line (- - -) represents the thermal noise I_T (eq 6) of the pore, the dash-dot (-· -· -·) line represents the noise of the headstage and amplifier I_A (eq 4), the dash-dot-dot (-· · -· · -· ·) line represents the dielectric noise of the substrate I_D (eq 8), the dotted line (· · ·) represents the quantization noise I_Q (eq S4 in the Supporting Information), and the solid line (—) represents the total noise I_{total} (*i.e.*, the rms sum of the four noise sources, eq 9). Note, quantization noise is very small and the dotted line lies in all panels on the *x*-axis. (B) Predicted noise from the four noise sources for the PET pores used in this work with $f_c = 40$ kHz. Note that dielectric noise is now larger than the headstage and amplifier noise. (C) Same graph as in panel A except with $f_c = 10$ kHz. (D) Same graph as in panel B except with $f_c = 10$ kHz. (E) Same graph as in panel A except with $f_c = 1$ kHz. (F) Same graph as in panel B except with $f_c = 1$ kHz.

Figure 3 shows the theoretical rms value of the noise generated by the headstage and amplifier with a headstage amplification of $\beta = 1$ (dash-dot line, -· -· -·). For comparison, we show in the Supporting Information the theoretical rms value of the noise generated by the headstage and amplifier when $\beta = 0.1$ (Figure S1). Figure 3 demonstrates that the headstage and amplifier contribute one of the most important sources of noise in current recordings when pores with resistances greater than ~30 to ~400 MΩ are used. Overall, we expect the noise of the headstage and amplifier to be significant (or dominant) in many current recordings from synthetic pores, especially in experiments that require high signal bandwidths (see the Supporting Information for methods to minimize the noise from the headstage and amplifier).

Theoretical Noise Generated by the Pore. To a first approximation, the overall pore structure can be considered as a simple resistive element. Resistors generate noise because of thermal agitation of charge carriers inside the device,[11] and this type of noise is known as thermal noise (also called Johnson noise or Nyquist noise).

The power spectral density of thermal noise $S_T^2(f)$ is given by eq 5 and the rms thermal noise $I_T(f_c)$ is given by eq 6:[10,11]

$$S_T^2(f) = \frac{4kT}{R} \quad (5)$$

$$I_T(f_c) = \sqrt{\frac{4kTc_1 f_c}{R}} \quad (6)$$

where R (Ω) is the resistance of the pore structure, k is Boltzmann's constant, 1.38×10^{-23} m^2 kg s^{-2} K^{-1}, and T (K) is the temperature (here $T = 294$ K). The dashed line (- - -) in Figure 3 shows the resulting theoretically estimated rms value of the thermal noise I_T as a function of the resistance of the pore structure for three different signal bandwidths using eq 6.

We propose that eqs 5 and 6 provide a reasonable approximation of the thermal noise that is generated by many of the pore structures that are commonly used for current recordings; however, if the capacitance of the substrate is large (greater than ~100 pF), or the resistance of the pore is large (greater than ~100 MΩ), or the resistance leading to and from the pore is large (greater than ~500 Ω), eqs 5 and 6 may no longer accurately describe the thermal noise of the pore structure. In this instance, it may be more accurate to derive the theoretical thermal noise equation of the pore from the model circuit of the pore (Figure 2) rather than using eqs 5 and 6.[10] For comparison, we present a general method for determining the thermal noise from the model circuit in the Supporting Information, and we used this method to derive thermal noise equations for the model circuits presented in Figure 2.

On the basis of Figure 3, we predict that the thermal noise generated by the pore structure is an important or dominant source of noise for both dielectric materials if the resistance of the pore is smaller than ~30 MΩ (at bandwidths less than 10 kHz, thermal noise dominates for pores with resistances up to ~400 MΩ). As a general rule, the thermal noise of the pore is the minimum amount of noise achievable in a current trace, and we expect that it will be a significant source of noise in many experiments (see the Supporting Information for strategies to perform resistive-pulse measurements with the optimal signal bandwidth in order to reduce the thermal noise to its minimum value without compromising the accuracy of resistive-pulse recordings).

Theoretical Noise Generated by the Substrate Material. Synthetic nanopores are typically fabricated in dielectric materials such as silicon dioxide, silicon nitride, glass, and polymers. While these materials provide excellent substrates that can be chemically and mechanically robust, they exhibit loss in the form of thermal energy. The thermal energy generated by this loss results in thermal noise from the dielectric material,[11] and this type of noise is known as dielectric noise. The power spectral density of dielectric noise $S_D^2(f)$ is given by eq 7 and the rms dielectric noise $I_D(f_c)$ is given by eq 8:[10,11]

$$S_D^2(f) = 8\pi\, kTDC_d f \quad (7)$$

$$I_D(f_c) = \sqrt{4\pi\, kTDC_d c_2 f_c^2} \quad (8)$$

where D is the dissipation factor (or dielectric loss tangent, unitless) of the material(s), and C_d (F) is the capacitance of the dielectric(s).

In general, D is determined by combining the dielectric loss of all materials that contribute to the capacitance C_d. These materials do not, however, contribute to D equally; thus it can be difficult to determine an exact value of D.[12] Since the pores that we used were made of a single substrate material, either glass or PET, (and the substrate did not require any form of support that made a significant contribution to C_d), we estimated D as the dielectric loss of the material in which the pore was fabricated (D is frequency dependent but usually changes minimally over the range of frequencies of interest here[11]). For the conical pores in Corning 0211 borosilicate glass, the value of D was 0.0047 and the capacitance of the dielectric was $C_d = C_s + C_m + C_c \approx 10$ pF.[150] For the cylindrical pores fabricated in PET, the value of D was 0.016 and the capacitance of the dielectric was $C_d = C_s \approx 30$ pF.[151] The dash dot dot line (- · · - · · - · · ·) in Figure 3 shows the theoretical rms value of the dielectric noise of the glass and PET pores for three signal bandwidths.

Figure 3 demonstrates that the increased capacitance and dissipation factor of the PET pores compared to the glass pores caused an increase in the dielectric noise of the substrate (as well as the noise of the headstage and amplifier). This analysis predicts that in the case of PET pores with resistances larger than ~30 MΩ and signal bandwidths greater than 10 kHz, dielectric noise is the largest source of noise. At bandwidths less than 10 kHz, dielectric noise dominates for pores with resistances larger than ~400 MΩ. This noise source can be particularly important for high signal bandwidth applications since the rms value of the dielectric noise grows linearly with the signal bandwidth (eq 8, see the Supporting Information for methods to reduce dielectric noise).

Theoretical Noise Generated by the Digitizer. Figure 3 shows that quantization noise $I_Q(f_c)$ (the main source of noise generated by a digitizer) is typically not an important source of noise. In most cases, we do not expect quantization noise to contribute significantly to the overall noise in a current trace; however, since this noise source is added after the current trace is filtered with an analog filter, it can be significant in current traces that have been strongly filtered with analog filters during the recordings. Therefore we present a detailed discussion of quantization noise, equations to predict quantization noise (we used these equations to determine $I_Q(f_c)$ in Figure 3), and methods to minimize quantization noise in the Supporting Information.

Calculation of the Total Theoretical rms Noise. The total theoretical rms value of the current noise can be calculated by considering the underlying random nature of the sources of noise. This randomness causes uncorrelated noise sources to add in an rms fashion.[11] Since the rms value of the thermal noise of the pore I_T, the dielectric noise of the substrate I_D, the noise of the amplifier I_A, and the quantization noise of the digitizer I_Q are uncorrelated, the total rms noise I_{total} is equal to

$$I_{total} = \sqrt{I_T^2 + I_D^2 + I_A^2 + I_Q^2} \qquad (9)$$

Owing to the rms addition of the sources of the noise, the largest source(s) of noise tends to dominate the total noise as shown in Figure 3. Considering this characteristic is crucial for attempts to reduce the noise of current recordings (see the Supporting Information for detailed recommendations on reducing the noise of current recordings).

To predict accurately the total rms noise, the noise bandwidth of each source must be determined. In general, the signal bandwidth of the *HAFD* combination (or *HAFD*-digital filter combination) should be used for calculating the noise bandwidth of the headstage and amplifier noise, the dielectric noise of the substrate, and the thermal noise of the pore.[152]

To summarize, Figure 3 shows that the total noise is dominated by thermal noise for PET and glass pores with resistances less than 30−400 MΩ. For glass pores with resistances greater than ~400 MΩ, the largest source of noise is the headstage and amplifier. For PET pores with resistances above ~400 MΩ, the largest source of noise is dielectric noise.

Effect of Substrate Capacitance on the Noise of Current Recordings. The capacitance of the substrate that contains the pore can have a significant effect on the noise of a current trace since it influences the noise of the headstage and amplifier, the dielectric noise of the substrate, and potentially the thermal noise of the pore (as discussed in the Supporting Information). To examine the effect of substrate capacitance, we plotted in Figure 4 the theoretical rms noise of the four individual sources as well as the total noise as a function of the substrate capacitance. Since we allowed the substrate capacitance to range from 10 pF to 2 nF, we estimated the thermal noise with an equation (eq S10) that takes into account the effect of the substrate capacitance (derived for cylindrical pores, Figure 2B); this equation and its derivation are provided in the Supporting Information. In Figure 4, we examine two scenarios, a "low-noise scenario" (D = 0.0047 and β = 1, Figure 4A,C,E) and a "high-noise scenario" (D = 0.016 and β = 0.1, Figure 4B,D,F) at three different signal bandwidths. In both scenarios, we found that the noise increased with increasing capacitance and that this increase was particularly strong at high signal bandwidths. It is therefore critical to obtain substrates with low capacitance (ideally below 100 pF) to perform recordings with low-noise at high signal bandwidths.[10,12,13,22]

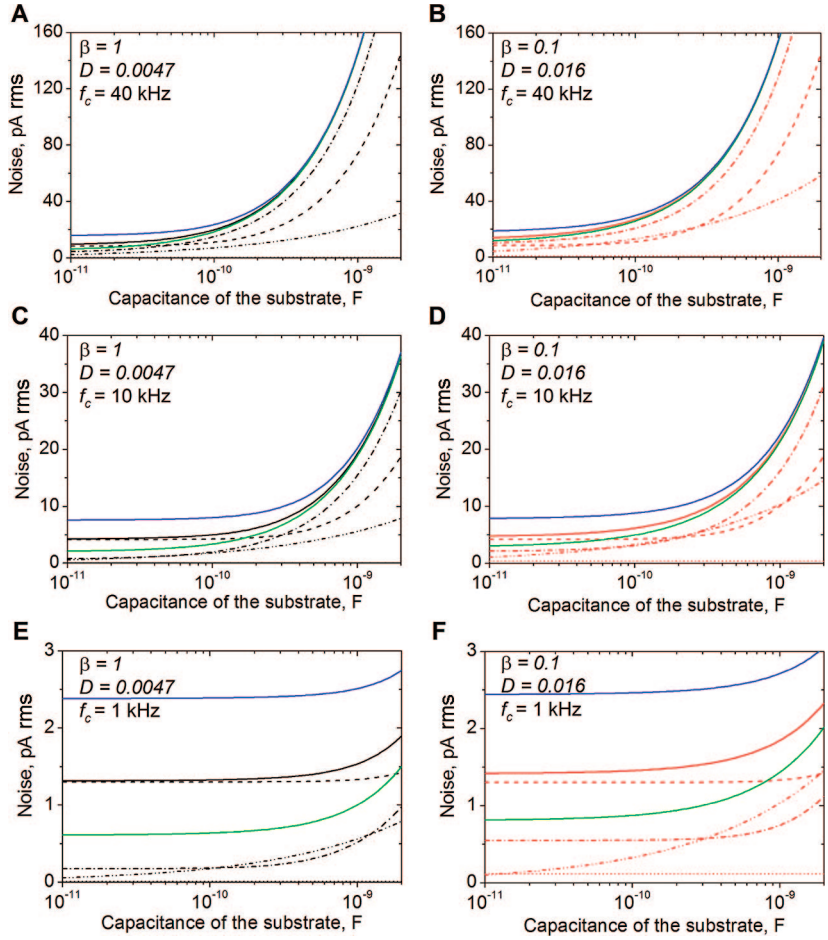

Figure 4. Magnitude of four theoretical noise sources and the total theoretical noise in current recordings from submicrometer pores and nanopores as a function of the capacitance of the substrate C_s. The graphs show the headstage and amplifier noise I_A (- - -, eq 4), the dielectric noise I_D (- · - · - · -, eq 8), the thermal noise $I_{T\text{-}Cyl}$ (- - -, eq S10 in the Supporting Information) derived for a cylindrical pore structure (Figure 2B), the quantization noise I_Q (· · ·, eq S4 in the Supporting Information), and the resulting total noise $I_{total\text{-}C}$ (—, which represents the rms sum of the preceding four noise sources) at three different signal bandwidths for a "low-noise" scenario (black curves) with D = 0.0047 and β = 1 and a "high-noise" scenario (red curves) with D = 0.016 and β = 0.1. The black and red curves in each plot were calculated for a pore with a resistance of R_p = 10 MΩ ($R_a = R_{w1} + R_{w2}$ = 350 Ω). The blue and green curves show the total noise for two additional resistance values of the pore: R_p = 3 MΩ (blue) and R_p = 50 MΩ (green). (A) Predicted noise at a signal bandwidth of 40 kHz for pores with a dielectric loss D = 0.0047, headstage gain β = 1 (R_f = 500 MΩ, C_a = 25 pF, and the overall gain of the amplifier G = 500 MV A^{-1}) and assuming no excess noise in the feedback resistor (a = 1). (B) Predicted noise at a signal bandwidth of 40 kHz for pores with a dielectric loss D = 0.016, headstage gain β = 0.1 (R_f = 50 MΩ, C_a = 70 pF, and G = 50 MV A^{-1}) and assuming no excess noise in the feedback resistor (a = 1). (C) Identical to graph as in panel A except with f_c = 10 kHz. (D) Identical to graph as in panel B except with f_c = 10 kHz. (E) Identical to graph as in panel A except with f_c = 1 kHz. (F) Identical to graph as in panel B except with f_c = 1 kHz.

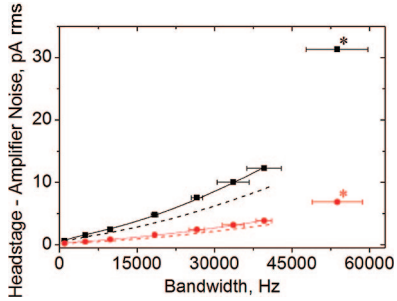

Figure 5. Noise generated by the combination of the headstage (no load applied to the input pins) with the patch clamp amplifier as a function of the bandwidth at two different settings of the gain: β = 0.1 (black) and β = 1 (red). All data points were obtained by selecting the signal bandwidth by digital filtering[154] except for the two points marked with an asterisk (which were obtained by analog filtering only). The dashed lines were calculated (not fitted) using eq 5 without consideration of excess noise ($a = 1$). The solid lines were generated by fitting eq 4 to the data using a and C_t (since there was no load attached, $C_t = C_a$) as fitting parameters. For β = 0.1, the best fit ($R^2 \geq 0.99$) generated a value of $a = 1.6$ and of $C_a = 98$ pF. For β = 1, the best fit ($R^2 \geq 0.99$) generated a value of $a = 1.9$ and of $C_a = 30$ pF. The points marked with an asterisk were excluded from the best fit analysis.[155]

Figure 4 provides a way to estimate (or extrapolate) the minimal predicted individual and total noise for most of the pores and experimental conditions that will be encountered in submicrometer pore- and nanopore-based current recordings. It encloses the following parameter range: resistance of the pore, 3 to 50 MΩ and capacitance of substrate, 10 pF to 2 nF.

Comparison of Theoretical and Experimental Noise of the Headstage and Amplifier. To test the accuracy of the theoretical equations of the noise of the headstage and amplifier, we compared the theoretically calculated values with experimental results. The power spectrum of the quantization noise was constant over the frequency range of interest as predicted by theory (see Supporting Information for a comparison of the theoretical and experimental quantization noise),[11] hence we were able to subtract the experimentally determined quantization noise from the measured value of the noise of the recording electronics. The resulting experimentally determined headstage and amplifier noise made it possible to compare the theoretical equations of the rms noise generated by the amplifier (no load applied to the input pins) with the measured rms noise from current traces that were filtered with digital Gaussian low-pass filters of varying cutoff frequency for β = 0.1 and β = 1 as shown in Figure 5.

Since the capacitance of the amplifier C_a and the constant representing excess noise in the feedback resistor a were not well defined, we carried out best fit analyses to the experimental data points with eq 4 by using C_a and a as fitting parameters (since no load was connected to the input pins, $C_a = C_t$). With this procedure, we obtained excellent fits for β = 0.1 with $C_a = 98$ pF and $a = 1.6$ as well as for β = 1 with $C_a = 30$ pF and $a = 1.9$ as shown in Figure 5.[153] In summary, the parameters from the best fit analysis made it possible to predict the noise from the headstage and amplifier with very high accuracy up to a signal bandwidth of 40 kHz.

A Combination of Theory and Experimental Results Enabled an Accurate Prediction of the Total Noise of Pores in Glass or PET Substrates. One of the main goals of this work was to enable the prediction of the expected noise of current recordings from pores with a variety of geometries that were fabricated in various materials. To this end, we demonstrate the accurate prediction of the experimentally observed noise of pores in glass or PET substrates. The pores in glass substrates that we used had conical geometry and diameters ranging from 250 nm to 1.5 μm (Figure 2A). The pores in PET substrates that we used had cylindrical geometry and diameters ranging from ~10 to 610 nm (Figure 2B). To predict the current noise, we used eq 9 with the following modifications to the individual sources of noise. For the headstage and amplifier noise, we used eq 4 with $C_a = 98$ pF and $a = 1.6$ for β = 0.1 and with $C_a = 30$ pF and $a = 1.9$ for β = 1 (as obtained from the best fits shown in Figure 5). For the quantization noise, we used the experimentally measured value since it was straightforward to determine and significantly greater than the theoretical value (as discussed in the Supporting Information). We used the thermal noise and dielectric noise equations as given by eqs. 6 and 8.

As shown in Figure 6, the predicted noise values and the measured values were in excellent agreement (error <5%), in particular for recordings at signal bandwidths below 24 kHz. Consequently, the theoretical approach described here can be used to predict accurately the expected noise from pores *before* fabricating these pores and *before* carrying out any experiments. This predicted, minimal achievable noise can be used to assess the best possible signal-to-noise ratio for resistive pulse recordings of objects that move through the submicrometer- or nanometer-sized pores by combining the analysis with theoretical equations for predicting the amplitudes from translocating objects.[17,22,73,74,84,89,127,128]

One surprising result from Figure 6 is that at the highest signal bandwidth (40 kHz), the pores in glass and in PET generated a measurable current noise that was slightly *smaller* than the theoretically predicted value (which we expected to be the minimal possible noise). For pores in glass the maximum difference between the measured and predicted noise value was ≤8.5%, and for the pores in PET it was ≤12% for either value of β. We think that these decreased experimental noise levels at the highest signal bandwidths were mainly due to small inaccuracies in the measurement of the signal bandwidth of the *HAFD*-digital filter combination.[156]

Application of a Voltage, in Some Cases, Increased the Noise of the Current Trace. Most of the experiments that use submicrometer pores and nanopores for sensing require the application of a voltage across the membrane to monitor the current flowing through the pore. The application of a voltage can, however, cause an increase in the noise of the current trace (in some cases, the noise can grow by more than one order of magnitude).[55,62,63,120] Therefore, we examined the noise for all pores used in this work while applying a voltage. Typical resistive-pulse sensing experiments use a voltage of 0.1−0.4 V.[1−6] Here we limit our discussion to pores that produced currents smaller than 200 nA (the saturation value of the amplifier) under voltage biases up to 0.4 V ($N = 17$). Figure 7 shows that in roughly half of the experiments, the noise increased significantly after a voltage was applied. For glass pores, the magnitude of the increase showed a weak dependence on the resistance of the pore with increased noise at low resistance values. For PET pores, we observed almost no change in the noise upon application of a voltage across the pore.

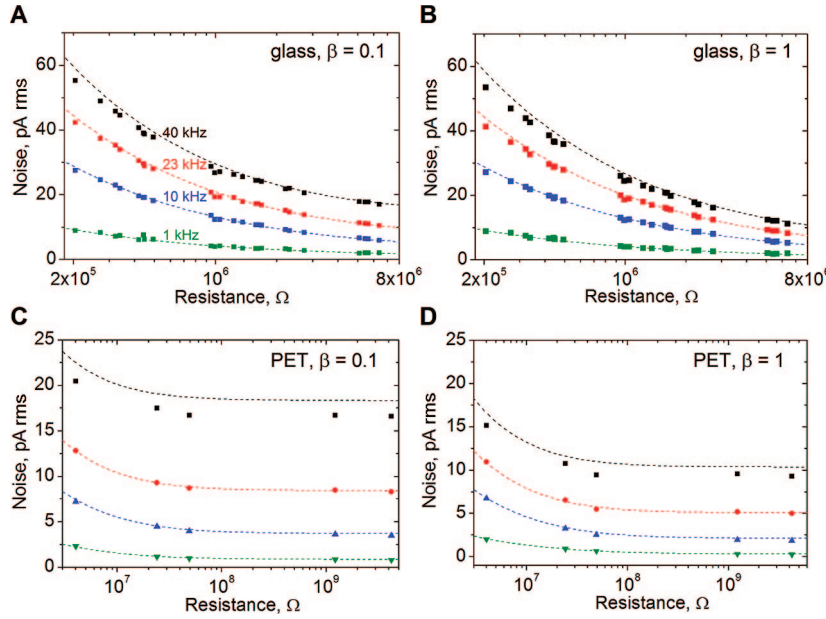

Figure 6. Comparison between predicted and measured noise of pores fabricated in glass and PET at four different signal bandwidth values (*i.e.*, the original current trace was filtered with a digital Gaussian low-pass filter with one of four specified cutoff frequencies). The signal bandwidth of the HALD-digital filter combination was determined experimentally from the t_{10-90} risetime; it was ~40 (black), ~23 (red), ~10 (blue), and ~1 kHz (green). The dashed lines were calculated using eq 9 with the modifications to the individual sources of noise as discussed in the text. (A) Predicted (dashed lines) and measured noise values (points) from conical pores in glass with diameters ranging from 250 nm to 1.5 μm as a function of the resistance of these pores with β = 0.1. (B) Identical graph as in panel A except with β = 1. (C) Noise values measured from cylindrical pores in PET with diameters ranging from ~10 to 610 nm as a function of the resistance of these pores (β = 0.1). (D) Identical graph as in panel C except with β = 1. The recording buffer for experiments with the glass pores was either 1.00 M KCl with 0.01 M phosphate buffer pH 7.3 and 0.1% w/v Triton X-100 or 0.15 M KCl with 0.01 M phosphate buffer pH 7.3 and 0.1% w/v Triton X-100; the recording buffer for the experiments with the PET pores was 1.00 M KCl with 0.01 M phosphate buffer pH 7.3 and 0.1% w/v Triton X-100. The applied voltage was 0.0 V in all cases.

In general, the noise generated by the headstage and amplifier, the quantization noise generated by the digitizer, the dielectric noise generated by the substrate, and the thermal noise generated by the pore are not expected to increase when a voltage is applied (or when current flows). So the question is, what caused the extra noise in an applied electric field? One possible source is shot noise.[11,131,133,157−161] The rms shot noise is usually modeled as increasing proportionately with the square root of the current, which would agree with the trend of increasing noise with decreasing resistance in glass pores; however, significant shot noise is only expected in circuits that contain a potential barrier (such as a diode or certain ion channels),[157,160,162] and the power spectral density of shot noise is independent of frequency.[10,157,162]

As far as we know, the glass pores used in this work did not contain a potential barrier (the double layer thickness was ~0.3 nm for the solution that contained 1 M KCL and ~0.8 nm for the solution that contained 0.15 M KCl; it was thus always significantly less than the diameter of the pore) and these pores did not exhibit rectification (both of these characteristics applied to the PET pores as well). Furthermore, as shown in Figure 8, the increase in the power of the noise under an applied voltage did not occur over the entire frequency range (*i.e.*, the increase in the power of the noise with an applied voltage was dependent on frequency). Therefore, we do not think that shot noise was the cause of the extra noise observed in glass pores.[163]

The frequency dependence shown in Figure 8 reveals a possible source of the extra noise. As the frequency decreased below approximately 50 kHz, the power of the noise from the current traces with an applied voltage increased linearly with decreasing frequency on a log−log plot whereas the power of the noise from the current trace without an applied voltage remained flat. Figure 8 also shows that the linear increase in noise power as a function of drecreasing frequency was maintained from the initial frequency at which the noise power began to increase (which varied from pore to pore) until the lowest frequencies on the power spectra (~6 Hz).[164] A linear increase of the noise power as a function of decreasing frequency in a double logarithmic plot is in agreement with so-called 1/*f* noise or flicker noise. This type of noise is characterized by a power spectrum S_F^2 of[134]

$$S_F^2 = \frac{c}{f^\alpha} \qquad (10)$$

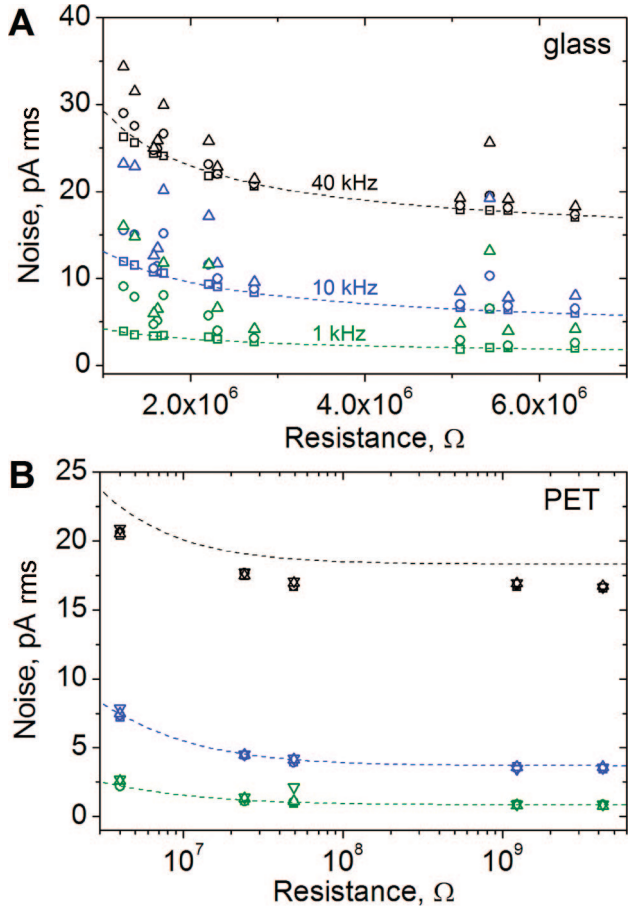

Figure 7. Influence of an applied voltage on the rms current noise recorded from pores in glass and PET substrates. (A) Noise measured with glass pores at a signal bandwidth of ~40 (black), ~10 (blue), and ~1 kHz (green) with an applied voltage of 0.0 (squares), 0.1 (circles), or 0.2 V (up triangles) with a headstage gain of β = 0.1. (B) Noise obtained from PET pores at a signal bandwidth of ~40 (black), ~10 (blue), and ~1 kHz (green) with an applied voltage of 0.0 (square), 0.1 (circles), 0.2 (up triangles), or 0.4 V (down triangles) with a headstage gain of β = 0.1. The recording buffer for the glass pores was either 1.00 M KCl with 0.01 M phosphate buffer pH 7.3 and 0.1% w/v Triton X-100 or 0.15 M KCl with 0.01 M phosphate buffer pH 7.3 and 0.1% w/v Triton X-100. The recording buffer for the PET pores was 1.00 M KCl with 0.01 M phosphate buffer pH 7.3 and 0.1% w/v Triton X-100.

where c (A^2) is a constant (and usually has the value 1) and α is close to 1. The value of α can vary considerably, and discussions on 1/*f* noise include values of α that range from 0 to 2.[134] Noise with the type of power spectra as shown in Figure 8 has been observed previously in nanopore structures that were fabricated in synthetic membranes,[55,62,63,120] and recent reports have proposed a physical origin including nanobubbles in the pore[62] or mobile surface charges on the surface of the walls of the pore for the generation of this noise.[55]

To examine if the extra noise that we found experimentally with glass pores had a 1/*f* origin, we fitted the power spectra of the current noise from these pores with eq 10 ($N = 12$, applied voltage of 0.2 V). We obtained good fits (in all but three cases R^2 was greater than 0.88) with values for c that varied between 0.2−8.4

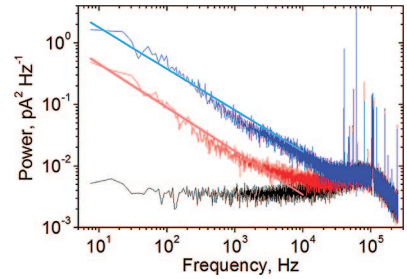

Figure 8. Representative power spectra of the current noise recorded from a glass pore that exhibited a large amount of extra noise under an applied voltage of 0.0 (black), 0.1 (red), 0.2 V (blue). The light blue and the light red line were generated by fitting the power spectra to eq 10. For the light red line, α was equal to 0.70 ± 0.01; for the light blue line, α was equal to 0.67 ± 0.01.

(average of 3.0 ± 2.4) and values for α that varied between 0.4−0.8 (average of 0.6 ± 0.1).

In summary, we suggest the extra noise generated by the glass pores used here was of a 1/*f* origin, although, at this point, we do not know the exact mechanism causing its generation. Overall, the occurrence of significant 1/*f* noise under conditions of an applied voltage appeared random from pore to pore. This variability has been described in other devices that display significant 1/*f* noise.[162] Generally, we (and others) do not conduct current recordings with pores that exhibit significant amounts of extra noise under an applied voltage since this noise reduces the sensitivity of the measurement (in our experience, these pores are also more prone to clogging compared to pores that do not have significant amounts of extra noise). Hence, for many experiments, the noise equations provided here can be used to predict accurately the noise from current recordings even in the presence of an applied voltage. Finally, while we attempted to provide an exhaustive list of sources of noise, there are other potential sources of noise (*e.g.*, vibration induced noise) and some may even be substrate specific (*e.g.*, light induced noise in silicon devices). These other sources of noise, if present, may need to be included in order to predict accurately the noise of a current recording.

CONCLUSION

On the basis of a detailed discussion of the signal bandwidth and noise of current recordings from individual submicrometer pores or nanopores, we show theoretically and experimentally that these two parameters can critically affect the sensitivity, accuracy, and information content from resistive-pulse sensing experiments (and other experiments that record the current through pores). The signal bandwidth limits the time resolution of changes in the current while the noise helps determine the sensitivity of a given pore. The signal bandwidth and noise are currently two of the limiting factors for experiments that attempt to sense the very small, often short-lived resistive-pulses (or fluctuations in these pulses) during the passage of individual

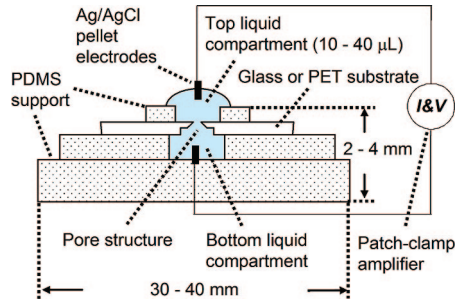

Figure 9. Sideview of the recording setup used for the experiments presented here.[27,49]

nucleobases through nanopores for applications such as DNA sequencing.[14] Detection of such short-lived events with small amplitude changes will either require new recording modalities with very low noise at extremely high-bandwidth or it will require strategies to increase significantly the amplitudes of resistive-pulses (possibly by fabricating pores with very small channel lengths and diameters) perhaps combined with a strategy to prolong the duration of pulses from individual bases (possibly by filling the pores with a chemically cross-linked sieving gel). At present, the bandwidth and noise pose a fundamental challenge to the tremendous potential of submicrometer pore- and nanopore-based sensing. This report is intended to provide most of the relevant parameters that may be helpful for realizing this potential.

EXPERIMENTAL SECTION

Solutions. We prepared all solutions with deionized water (resistivity of 18.2 MΩ cm, Millipore, Billerica, MA), and we used all chemicals without further purification, including potassium chloride, sulfuric acid (both from EMD Biosciences, La Jolla, CA), bovine serum albumin, Triton X-100 (both from Sigma Chemical Company, St Louis, MO), tris(hydroxymethyl)aminomethane (TRIS, Shelton Scientific, Shelton, CT), potassium phosphate—monobasic, potassium phosphate—dibasic (both from J.T. Baker, Phillipsburg, NJ), hydrochloric acid (VWR International, West Chester, PA), nitric acid (Fluka Chemie, Buchs, Switzerland), and hydrogen peroxide (EMD Chemicals, Gibbstown, NJ). Recording buffer for the noise measurements, which consisted of either 0.15 M KCl with 0.01 M phosphate buffer pH 7.3 and 0.1% w/v Triton X-100 or 1.00 M KCl with 0.01 M phosphate buffer pH 7.3 and 0.1% w/v Triton X-100, was filtered through sterile 0.1 or 0.2 μm polyethersulfone membrane filters (both from Pall, East Hills, NY). Recording buffer for the virus experiment, which consisted of 0.15 M KCl with 0.05 M tris(hydroxymethyl)aminomethane (TRIS) buffer pH 7.8 and 0.1 mg mL^{-1} bovine serum albumin as well as 0.1% w/v Tween 20, was filtered through sterile 0.2 μm polyethersulfone membrane filters.

Pore Fabrication and Imaging. We fabricated glass pores with conical geometry using a femtosecond-pulsed laser as described previously.[27,49] Briefly, we attached a glass coverslide (Corning 0211 borosilicate, Fisher Scientific, Pittsburgh, PA) to a 3-axes microscope nanomanipulation stage (Mad City Laboratories, Inc., Madison, WI), and placed a droplet of water on the area that was to be machined. For laser-based ablation of the glass at defined locations, we focused a directly diode-pumped Nd:glass CPA laser system (Intralase Corp., Irvine, CA) through a 100 × oil immersion microscope objective (N.A. = 1.3, Zeiss, Thornwood, NY), and used laser pulses that were frequency doubled from 1053 to 527 nm with a duration of 600−800 fs.[165–168] To fabricate the pore, we used a three-stage machining process that employed different pulse energy and repetition rates for the cylindrical shank that was 35 μm wide (see Figure 2A), top of the cone, and tip of the cone. Polyethylene terephthalate (PET) pores with cylindrical geometry and with diameters ranging from 10 to 610 nm were kindly provided by Professor Zuzanna S. Siwy, University of Irvine, CA; we used these pores without further cleaning or treatment.

After fabrication, we coated the glass pores in gold (thickness of ~10 nm) using a sputter coater (Structure Probe Incorporated, West Chester, PA) and imaged them with a high resolution scanning electron microscope (HRSEM, FEI Company NOVA 200 Nanolab, Hillsboro, OR). Before using these pores for experiments, we removed the gold layer by etching in a 3:1 (vol/vol) mixture of fuming nitric acid and concentrated hydrochloric acid. In some cases, we reduced the diameters of the glass pores by depositing silicon dioxide at 380 °C using plasma enhanced chemical vapor deposition (PECVD, Group Sciences Inc., San Jose, CA). The deposition time varied from pore to pore but was always less than 60 s. Before each experiment, we cleaned the glass pores in a fresh 3:1 (vol/vol) mixture of concentrated sulfuric acid with 30% hydrogen peroxide for at least 15 min.

Data Acquisition. To assemble the recording setup, we placed the glass substrate with the pore or the PET substrate with the pore on a fluidic channel in poly(dimethylsiloxane) (PDMS, Sylgard 184 Silicone, Dow Corning, Midland, MI).[27,49] We used a fresh film of PDMS (thickness, ~1 mm) with a hole in the center (diameter, ~3.6 mm) to confine the electrolyte (recording buffer) in the top liquid compartment as shown in Figure 9. We placed the PDMS-pore assembly inside a Faraday cage (Warner Instruments, Hamden, CT) that had solid walls; therefore, no light penetrated the interior. To guarantee reliable recording conditions while measuring the wide range of currents (10^{-9} to 10^{-12} A) in the experiments, we used Ag/AgCl pellet electrodes (Eastern Scientific, Rockville, MD). For recording currents at constant voltage, we used a patch clamp amplifier (Axopatch 200B, Molecular Devices, Sunnyvale, CA) in voltage clamp mode with a gain of $\alpha = 0.5$ and with the built in, four-pole, analog low-pass Bessel filter set to a cutoff frequency of 100 kHz unless otherwise specified in the text. A low- noise digitizer (Digidata 1322, Molecular Devices) performed analog to digital data conversion with a sampling frequency f_s of 500 kHz, and we stored the data on a computer using recording software (Clampex 9.2, Molecular Devices).

Data Processing. We used the digital Gaussian low-pass filter provided with the Clampfit 9.2 software (Molecular Devices) with cutoff frequencies as specified in the text. This digital filter was always applied to the *original* current traces (as opposed to previously digitally filtered traces). We calculated noise power spectra using Clampfit 9.2 software. To measure root-mean-square (rms) values of the noise, we calculated the standard deviation of a current trace containing 50 ms of data (25,000 samples). We analyzed the noise data and performed all fitting operations using Origin 7.5 software (OriginLab, Northampton, MA). Theoretical calculations of the noise were performed using custom Matlab programs (The Mathworks, Natick, MA).

Recording Resistive-Pulses from Virus Particles. We followed the procedure described previously[49] to monitor resistive-pulses from virus particles. Briefly, we diluted concentrated *Paramecium Busaria* Chlorella Virus (PBCV-1), kindly provided by J. L. Van Etten, University of Nebraska-Lincoln, Lincoln, NE, in the recording buffer for the virus experiments to a final concentration of ~5×10^8 particles mL^{-1}. We then recorded resistive-pulses from virus particles passing through a glass pore with conical geometry and a diameter of ~650 nm under an applied potential of 0.2 V.

Measurement of the Signal Bandwidth of the Recording Electronics. To measure the signal bandwidth of the recording electronics (headstage, patch-clamp amplifier, analog low-pass filter, and digitizer), we used a high-quality function generator (Agilent 33220A, Agilent Technologies, Santa Clara, CA) to create a 2 kHz triangle waveform with a transition time from positive to nega-

tive slope of less than 0.5 μs. We then brought the two terminals of the function generator (signal and ground) within a few centimeters of the headstage and the ground input (or to the Ag-AgCl electrodes that were connected to these pins when the device was loaded with a glass or PET pore). The air gap between these components acted as a capacitor, and the current I flowing through a capacitor with a capacitance C is the time derivative of the input waveform of the voltage V ($I = C \times dV/dt$). Thus the input pins (or the electrodes connected to these pins) sensed a square wave with the same frequency as the triangle wave.

With this setup, we were able to measure the 10−90% risetime t_{10-90} of the recording electronics (*i.e.*, the time it took for the recorded square wave to go from 10% of its final value to 90% of its final value). This t_{10-90} risetime could be combined with eq 2 to calculate the signal bandwidth of the recording electronics.[11,131] We used the same technique to determine the signal bandwidth of the recording electronics after "loading" the setup (*i.e.*, after mounting a pore in the fluidic setup and immersing the electrodes in the two electrolyte compartments which were separated by a glass or PET substrate that contained a pore). We also used this capacitive coupling method to determine the signal bandwidth of the combination of the recording electronics with low-pass digital Gaussian filters by measuring the t_{10-90} risetime of the square wave after it was digitally filtered.

Acknowledgment. This material is based upon work supported by a National Science Foundation CAREER Award (M.M., Grant No. 0449088) and by a research grant from IMRA America and AISIN USA. The authors thank Alan J. Hunt and Zuzanna S. Siwy for providing synthetic membranes that contained a single submicrometer pore or nanopore. The authors also thank Daniel J. Estes, Toni Figl, Ken Healy, Ralph M. M. Smeets, and Vincent Tabard-Cossa for valuable discussions.

Supporting Information Available: Additional graphs of the theoretical noise of the glass and PET pores when $\beta = 0.1$, detailed analysis of the theoretical and experimental quantization noise, recommendations for minimizing the noise of the current recordings, recommendations for obtaining optimal current recordings for resistive-pulse sensing experiments, and detailed theoretical analysis of the thermal current noise of cylindrical pores and conical pores. This material is available free of charge *via* the Internet at http://pubs.acs.org.

REFERENCES AND NOTES

1. Choi, Y.; Baker, L. A.; Hillebrenner, H.; Martin, C. R. Biosensing with Conically Shaped Nanopores and Nanotubes. *Phys. Chem. Chem. Phys.* **2006**, *8*, 4976–4988.
2. Henriquez, R. R.; Ito, T.; Sun, L.; Crooks, R. M. The Resurgence of Coulter Counting for Analyzing Nanoscale Objects. *Analyst* **2004**, *129*, 478–482.
3. Bayley, H.; Martin, C. R. Resistive-Pulse Sensing - from Microbes to Molecules. *Chem. Rev.* **2000**, *100*, 2575–2594.
4. Deamer, D. W.; Branton, D. Characterization of Nucleic Acids by Nanopore Analysis. *Acc. Chem. Res.* **2002**, *35*, 817–825.
5. Seidel, R.; Dekker, C. Single-Molecule Studies of Nucleic Acid Motors. *Curr. Opin. Struct. Biol.* **2007**, *17*, 80–86.
6. Bayley, H. Sequencing Single Molecules of DNA. *Curr. Opin. Chem. Biol.* **2006**, *10*, 628–637.
7. Blake, S.; Mayer, T.; Mayer, M.; Yang, J. Monitoring Chemical Reactions by Using Ion Channel-Forming Peptides. *ChemBioChem* **2006**, *7*, 433–435.
8. Capone, R.; Blake, S.; Restrepo, M. R.; Yang, J.; Mayer, M. Designing Nanosensors Based on Charged Derivatives of Gramicidin A. *J. Am. Chem. Soc.* **2007**, *129*, 9737–9745.
9. Mayer, M.; Semetey, V.; Gitlin, I.; Yang, J.; Whitesides, G. M. Using Ion Channel-Forming Peptides to Quantify Protein-Ligand Interactions. *J. Am. Chem. Soc.* **2008**, *130*, 1453–1465.
10. Benndorf, K. Low-Noise Recording In *Single-Channel Recording*, 2nd ed.; Sakmann, B., Neher, E., Eds.; Plenum Press: New York, 1995; pp 129−153..
11. Sherman-Gold, R. *The Axon Guide*; Axon Instruments, Inc.: 1993.
12. Mayer, M.; Kriebel, J. K.; Tosteson, M. T.; Whitesides, G. M. Microfabricated Teflon Membranes for Low-Noise Recordings of Ion Channels in Planar Lipid Bilayers. *Biophys. J.* **2003**, *85*, 2684–2695.
13. Levis, R. A.; Rae, J. L. Low-Noise Patch-Clamp Techniques. *Methods Enzymol.* **1998**, *293*, 218–266.
14. Kasianowicz, J. J.; Brandin, E.; Branton, D.; Deamer, D. W. Characterization of Individual Polynucleotide Molecules Using a Membrane Channel. *Proc. Natl. Acad. Sci. U.S.A.* **1996**, *93*, 13770–13773.
15. Gu, L.; Braha, O.; Conlan, S.; Cheley, S.; Bayley, H. Stochastic Sensing of Organic Analytes by a Pore-Forming Protein Containing a Molecular Adapter. *Nature* **1999**, *398*, 686–690.
16. Fertig, N.; Tilke, A.; Blick, R. H.; Kotthaus, J. P.; Behrends, J. C.; Bruggencate, G. Stable Integration of Isolated Cell Membrane Patches in a Nanomachined Aperture. *Appl. Phys. Lett.* **2000**, *77*, 1218–1220.
17. Saleh, O. A.; Sohn, L. L. Quantitative Sensing of Nanoscale Colloids Using a Microchip Coulter Counter. *Rev. Sci. Instrum.* **2001**, *72*, 4449–4451.
18. Apel, P. Y.; Korchev, Y. E.; Siwy, Z.; Spohr, R.; Yoshida, M. Diode-Like Single-Ion Track Membrane Prepared by Electro-Stopping. *Nucl. Instrum. Methods Phys. Res., Sect. B* **2001**, *184*, 337–346.
19. Li, J.; Stein, D.; McMullan, C.; Branton, D.; Aziz, M. J.; Golovchenko, J. A. Ion-Beam Sculpting at Nanometre Length Scales. *Nature* **2001**, *412*, 166–169.
20. Harrell, C. C.; Lee, S. B.; Martin, C. R. Synthetic Single-Nanopore and Nanotube Membranes. *Anal. Chem.* **2003**, *75*, 6861–6867.
21. Storm, A. J.; Chen, J. H.; Ling, X. S.; Zandbergen, H. W.; Dekker, C. Fabrication of Solid-State Nanopores with Single-Nanometre Precision. *Nat. Mater.* **2003**, *2*, 537–540.
22. Ito, T.; Sun, L.; Crooks, R. M. Simultaneous Determination of the Size and Surface Charge of Individual Nanoparticles Using a Carbon Nanotube-Based Coulter Counter. *Anal. Chem.* **2003**, *75*, 2399–2406.
23. Saleh, O. A.; Sohn, L. L. Direct Detection of Antibody-Antigen Binding Using an on-Chip Artificial Pore. *Proc. Natl. Acad. Sci. U.S.A.* **2003**, *100*, 820–824.
24. Chang, H.; Kosari, F.; Andreadakis, G.; Alam, M. A.; Vasmatzis, G.; Bashir, R. DNA-Mediated Fluctuations in Ionic Current through Silicon Oxide Nanopore Channels. *Nano Lett.* **2004**, *4*, 1551–1556.
25. Heng, J. B.; Ho, C.; Kim, T.; Timp, R.; Aksimentiev, A.; Grinkova, Y. V.; Sligar, S.; Schulten, K.; Timp, G. Sizing DNA Using a Nanometer-Diameter Pore. *Biophys. J.* **2004**, *87*, 2905–2911.
26. Berkane, E.; Orlik, F.; Charbit, A.; Danelon, C.; Fournier, D.; Benz, R.; Winterhalter, M. Nanopores: Maltoporin Channel as a Sensor for Maltodextrin and Lamda-Phage. *J. Nanobiotechnol* **2005**, *3:3*.
27. Uram, J. D.; Ke, K.; Hunt, A. J.; Mayer, M. Label-Free Affinity Assays by Rapid Detection of Immune Complexes in Submicrometer Pores. *Angew. Chem., Int. Ed.* **2006**, *45*, 2281–2285.
28. Wu, M. Y.; Krapf, D.; Zandbergen, M.; Zandbergen, H. W.; Batson, P. E. Formation of Nanopores in Sin/Sio2 Membrane with an Electron Beam. *Appl. Phys. Lett.* **2005**, *87*, 113106.
29. Chang, H.; Iqbal, S. M.; Stach, E. A.; King, A. H.; Zaluzec, N. J.; Bashir, R. Fabrication and Characterization of Solid-State Nanopores Using a Field Emission Scanning Electron Microscope. *Appl. Phys. Lett.* **2006**, *88*, 103109.
30. Harrell, C. C.; Siwy, Z. S.; Martin, C. R. Conical Nanopore Membranes: Controlling the Nanopore Shape. *Small* **2006**, *2*, 194–198.
31. Wei, C.; Bard, A. J.; Feldberg, S. W. Current Rectification at Quartz Nanopipet Electrodes. *Anal. Chem.* **1997**, *69*, 4627–4633.

32. Karhanek, M.; Kemp, J. T.; Pourmand, N.; Davis, R. W.; Webb, C. D. Single DNA Molecule Detection Using Nanopipettes and Nanoparticles. *Nano Lett.* **2005**, *5*, 403–407.
33. Benndorf, K. Properties of Single Cardiac Na Channels at 35 Degrees C. *J. Gen. Physiol.* **1994**, *104*, 801–820.
34. Danelon, C.; Santschi, C.; Brugger, J.; Vogel, H. Fabrication and Functionalization of Nanochannels by Electron-Beam-Induced Silicon Oxide Deposition. *Langmuir* **2006**, *22*, 10711–10715.
35. Wu, S.; Park, S. R.; Ling, X. S. Lithography-Free Formation of Nanopores in Plastic Membranes Using Laser Heating. *Nano Lett.* **2006**, *6*, 2571–2576.
36. Quist, A. P.; Chand, A.; Ramachandran, S.; Daraio, C.; Jin, S.; Lal, R. Atomic Force Microscopy Imaging and Electrical Recording of Lipid Bilayers Supported over Microfabricated Silicon Chip Nanopores: Lab-on-a-Chip System for Lipid Membranes and Ion Channels. *Langmuir* **2007**, *23*, 1375–1380.
37. Harrell, C. C.; Choi, Y.; Horne, L. P.; Baker, L. A.; Siwy, Z. S.; Martin, C. R. Resistive-Pulse DNA Detection with a Conical Nanopore Sensor. *Langmuir* **2006**, *22*, 10837–10843.
38. Kim, M. J.; Wanunu, M.; Bell, D. C.; Meller, A. Rapid Fabrication of Uniformly Sized Nanopores and Nanopore Arrays for Parallel DNA Analysis. *Adv. Mater.* **2006**, *18*, 3149–3153.
39. Park, S. R.; Peng, H.; Ling, X. S. Fabrication of Nanopores in Silicon Chips Using Feedback Chemical Etching. *Small* **2007**, *3*, 116–119.
40. Siwy, Z.; Apel, P.; Baur, D.; Dobrev, D. D.; Korchev, Y. E.; Neumann, R.; Spohr, R.; Trautmann, C.; Voss, K. Preparation of Synthetic Nanopores with Transport Properties Analogous to Biological Channels. *Surf. Sci.* **2003**, *532−535*, 1061–1066.
41. Schmidt, C.; Mayer, M.; Vogel, H. A Chip-Based Biosensor for the Functional Analysis of Single Ion Channels. *Angew. Chem., Int. Ed.* **2000**, *39*, 3137–3140.
42. Cai, Q.; Ledden, B.; Krueger, E.; Golovchenko, J. A.; Li, J. Nanopore Sculpting with Noble Gas Ions. *J. Appl. Phys.* **2006**, *100*, 024914.
43. Mitsui, T.; Stein, D.; Kim, Y. R.; Hoogerheide, D.; Golovchenko, J. A. Nanoscale Volcanoes: Accretion of Matter at Ion-Sculpted Nanopores. *Phys. Rev. Lett.* **2006**, *96*, 036102.
44. Sun, L.; Crooks, R. M. Single Carbon Nanotube Membranes: A Well-Defined Model for Studying Mass Transport through Nanoporous Materials. *J. Am. Chem. Soc.* **2000**, *122*, 12340–12345.
45. Kovarik, M. L.; Jacobson, S. C. Attoliter-Scale Dispensing in Nanofluidic Channels. *Anal. Chem.* **2007**, *79*, 1655–1660.
46. Wharton, J. E.; Jin, P.; Sexton, L. T.; Horne, L. P.; Sherrill, S. A.; Mino, W. K.; Martin, C. R. A Method for Reproducibly Preparing Synthetic Nanopores for Resistive-Pulse Biosensors. *Small* **2007**, *3*, 1424–1430.
47. von Schulthess, G. K.; Benedek, G. B.; DeBlois, R. W. Measurement of the Cluster Size Distributions for High Functionality Antigens Cross-Linked by Antibody. *Macromolecules* **1980**, *13*, 939–945.
48. von Schulthess, G. K.; Benedek, G. B.; DeBlois, R. W. Experimental Measurements of the Temporal Evolution of Cluster Size Distributions for High-Functionality Antigens Cross-Linked by Antibody. *Macromolecules* **1983**, *16*, 434–440.
49. Uram, J. D.; Ke, K.; Hunt, A. J.; Mayer, M. Submicrometer Pore-Based Characterization and Quantification of Antibody-Virus Interactions. *Small* **2006**, *2*, 967–972.
50. Siwy, Z. S. Ion-Current Rectification in Nanopores and Nanotubes with Broken Symmetry. *Adv. Funct. Mater.* **2006**, *16*, 735–746.
51. Siwy, Z. S.; Heins, E.; Harrell, C. C.; Kohli, P.; Martin, C. R. Conical-Nanotube Ion-Current Rectifiers: The Role of Surface Charge. *J. Am. Chem. Soc.* **2004**, *126*, 10850–10851.
52. Siwy, Z. S.; Powell, M. R.; Kalman, E.; Astumian, R. D.; Eisenberg, R. S. Negative Incremental Resistance Induced by Calcium in Asymmetric Nanopores. *Nano Lett.* **2006**, *6*, 473–477.
53. Siwy, Z. S.; Powell, M. R.; Petrov, A.; Kalman, E.; Trautmann, C.; Eisenberg, R. S. Calcium-Induced Voltage Gating in Single Conical Nanopores. *Nano Lett.* **2006**, *6*, 1729–1734.
54. Siwy, Z.; Fulinski, A. Fabrication of a Synthetic Nanopore Ion-Pump. *Phys. Rev. Lett.* **2002**, *89*, 198103.
55. Siwy, Z. S.; Fulinski, A. 1/F Noise in Ion Transport through Nanopores: Origins and Mechanism. *AIP Conf. Proc.* **2003**, *665*, 273–282.
56. Luchian, T.; Shin, S. H.; Bayley, H. Kinetics of a Three-Step Reaction Observed at the Single-Molecule Level. *Angew. Chem., Int. Ed.* **2003**, *42*, 1926–1929.
57. Shin, S. H.; Bayley, H. Stepwise Growth of a Single Polymer Chain. *J. Am. Chem. Soc.* **2005**, *127*, 10462–10463.
58. Uram, J. D.; Mayer, M. Estimation of Solid Phase Affinity Constants Using Resistive-Pulses from Functionalized Nanoparticles. *Biosens. Bioelectron.* **2007**, *22*, 1556–1560.
59. Siwy, Z.; Trofin, L.; Kohli, P.; Baker, L. A.; Trautmann, C.; Martin, C. R. Protein Biosensors Based on Biofunctionalized Conical Gold Nanotubes. *J. Am. Chem. Soc.* **2005**, *127*, 5000–5001.
60. Howorka, S.; Nam, J.; Bayley, H.; Kahne, D. Stochastic Detection of Monovalent and Bivalent Protein-Ligand Interactions. *Angew. Chem., Int. Ed.* **2004**, *43*, 842–846.
61. Keyser, U. F.; Krapf, D.; Koeleman, B. N.; Smeets, R. M. M.; Dekker, N. H.; Dekker, C. Nanopore Tomography of a Laser Focus. *Nano Lett.* **2005**, *5*, 2253–2256.
62. Smeets, R. M. M.; Keyser, U. F.; Wu, M. Y.; Dekker, N. H.; Dekker, C. Nanobubbles in Solid-State Nanopores. *Phys. Rev. Lett.* **2006**, *97*, 088101.
63. Chen, P.; Mitsui, T.; Farmer, D. B.; Golovchenko, J.; Gordon, R. G.; Branton, D. Atomic Layer Deposition to Fine-Tune the Surface Properties and Diameters of Fabricated Nanopores. *Nano Lett.* **2004**, *4*, 1333–1337.
64. Shin, S. H.; Luchian, T.; Cheley, S.; Braha, O.; Bayley, H. Kinetics of a Reversible Covalent-Bond-Forming Reaction Observed at the Single-Molecule Level. *Angew. Chem., Int. Ed.* **2002**, *41*, 3707–3709.
65. Luchian, T.; Shin, S. H.; Bayley, H. Single-Molecule Covalent Chemistry with Spatially Separated Reactants. *Angew. Chem., Int. Ed.* **2003**, *42*, 3766–3771.
66. Karnik, R.; Duan, C.; Castelino, K.; Daiguji, H.; Majumdar, A. Rectification of Ionic Current in a Nanofluidic Diode. *Nano Lett.* **2007**, *7*, 547–551.
67. Vlassiouk, I.; Siwy, Z. S. Nanofluidic Diode. *Nano Lett.* **2007**, *7*, 552–556.
68. Howorka, S.; Cheley, S.; Bayley, H. Sequence-Specific Detection of Individual DNA Strands Using Engineered Nanopores. *Nat. Biotechnol.* **2001**, *19*, 636–639.
69. Saleh, O. A.; Sohn, L. L. An Artificial Nanopore for Molecular Sensing. *Nano Lett.* **2003**, *3*, 37–38.
70. Bezrukov, S. M.; Kasianowicz, J. J. Dynamic Partitioning of Neutral Polymers into a Single Ion Channel In *Structure and Dynamics of Confined Polymers*; Kasianowicz, J. J., Kellermayer, M. S. Z., Deamer, D. W., Eds.; Kluwer Academic Publishers: Norwell, MA, 2002; pp 117−130..
71. Bezrukov, S. M.; Vodyanoy, I.; Parsegian, V. A. Counting Polymers Moving through a Single Ion Channel. *Nature* **1994**, *370*, 279–281.
72. Li, J.; Gershow, M.; Stein, D.; Brandin, E.; Golovchenko, J. A. DNA Molecules and Configurations in a Solid State Nanopore Microscope. *Nat. Mater.* **2003**, *2*, 611–615.
73. DeBlois, R. W.; Bean, C. P. Counting and Sizing of Submicron Particles by the Resistive Pulse Technique. *Rev. Sci. Instrum.* **1970**, *41*, 909–916.
74. Anderson, J. L.; Quinn, J. A. The Relationship between Particle Size and Signal in Coulter-Type Counters. *Rev. Sci. Instrum.* **1971**, *42*, 1257–1258.
75. DeBlois, R. W.; Bean, C. P.; Wesley, R. K. A. Electrokinetic Measurements with Submicron Particles and Pores by the Resistive Pulse Technique. *J. Colloid Interface Sci.* **1977**, *61*, 323–335.

76. Ito, T.; Sun, L.; Bevan, M. A.; Crooks, R. M. Comparison of Nanoparticle Size and Electrophoretic Mobility Measurements Using a Carbon-Nanotube-Based Coulter Counter, Dynamic Light Scattering, Transmission Electron Microscopy, and Phase Analysis Light Scattering. *Langmuir* **2004**, *20*, 6940–6945.
77. Lee, S.; Zhang, Y.; White, H. S.; Harrell, C. C.; Martin, C. R. Electrophoretic Capture and Detection of Nanoparticles at the Opening of a Membrane Pore Using Scanning Electrochemical Microscopy. *Anal. Chem.* **2004**, *76*, 6108–6115.
78. Ouali, L.; Stoll, S.; Pefferkorn, E.; Elaissari, A.; Lanet, V.; Pichot, C.; Mandrand, B. Coagulation of Antibody-Sensitized Latexes in the Presence of Antigen. *Poly. Adv. Technol.* **1995**, *6*, 541–546.
79. Pefferkorn, E.; Varoqui, R. Dynamics of Latex Aggregation - Modes of Cluster Growth. *J. Chem. Phys.* **1989**, *91*, 5679–5686.
80. DeBlois, R. W.; Wesley, R. K. A. Sizes and Concentrations of Several Type C Oncornaviruses and Bacteriophage T2 by the Resistive-Pulse Technique. *J. Virol.* **1977**, *23*, 227–233.
81. DeBlois, R. W.; Uzgiris, E. E.; Cluxton, D. H.; Mazzone, H. M. Comparative Measurements of Size and Polydispersity of Several Insect Viruses. *Anal. Biochem.* **1978**, *90*, 273–288.
82. Feuer, B. I.; Uzgiris, E. E.; Deblois, R. W.; Cluxton, D. H.; Lenard, J. Length of Glycoprotein Spikes of Vesicular Stomatitis Virus and Sindbis Virus, Measured *in Situ* Using Quasi Elastic Light Scattering and a Resisitve-Pulse Technique. *Virology* **1978**, *90*, 156–161.
83. Sauer-Budge, A. F.; Nyamwanda, J. A.; Lubensky, D. K.; Branton, D. Unzipping Kinetics of Double-Stranded DNA in a Nanopore. *Phys. Rev. Lett.* **2003**, *90*, 238101.
84. Aksimentiev, A.; Heng, J. B.; Timp, G.; Schulten, K. Microscopic Kinetics of DNA Translocations through Synthetic Nanopores. *Biophys. J.* **2004**, *87*, 2086–2097.
85. Mara, A.; Siwy, Z.; Trautmann, C.; Wan, J.; Kamme, F. An Asymmetric Polymer Nanopore for Single Molecule Detection. *Nano Lett.* **2004**, *4*, 497–501.
86. Chen, P.; Gu, J.; Brandin, E.; Kim, Y.; Wang, Q.; Branton, D. Probing Single DNA Molecule Transport Using Fabricated Nanopores. *Nano Lett.* **2004**, *4*, 2293–2298.
87. Storm, A. J.; Chen, J. H.; Zandbergen, H. W.; Dekker, C. Translocation of Double-Strand DNA through a Silicon Oxide Nanopore. *Phys. Rev. E* **2005**, *71*, 051903.
88. Storm, A. J.; Storm, C.; Chen, J.; Xandbergen, H.; Joanny, J.; Dekker, C. Fast DNA Translocation through a Solid-State Nanopore. *Nano Lett.* **2005**, *5*, 1193–1197.
89. Smeets, R. M. M.; Keyser, U. F.; Krapf, D.; Wu, M.; Dekker, N. H.; Dekker, C. Salt Dependence of Ion Transport and DNA Translocation through Solid-State Nanopores. *Nano Lett.* **2006**, *6*, 89–95.
90. Fan, R.; Karnik, R.; Yue, M.; Li, D.; Majumdar, A.; Yang, P. DNA Translocation in Inorganic Nanotubes. *Nano Lett.* **2005**, *5*, 1633–1637.
91. Meller, A.; Nivon, L.; Branton, D. Voltage-Driven DNA Translocations through a Nanopore. *Phys. Rev. Lett.* **2001**, *86*, 3435–3438.
92. Meller, A.; Nivon, L.; Brandin, E.; Golovchenko, J.; Branton, D. Rapid Nanopore Discrimination between Single Polynucleotide Molecules. *Proc. Natl. Acad. Sci. U.S.A.* **2000**, *97*, 1079–1084.
93. Meller, A.; Branton, D. Single Molecule Measurements of DNA Transport through a Nanopore. *Electrophoresis* **2002**, *23*, 2583–2591.
94. Bates, M.; Burns, M.; Meller, A. Dynamics of DNA Molecules in a Membrane Channel Probed by Active Control Techniques. *Biophys. J.* **2003**, *84*, 2366–2372.
95. Mathe, J.; Visram, H.; Viasnoff, V.; Rabin, Y.; Meller, A. Nanopore Unzipping of Individual DNA Hairpin Molecules. *Biophys. J.* **2004**, *87*, 3205–3212.
96. Keyser, U. F.; Koeleman, B. N.; Van Dorp, S.; Krapf, D.; Smeets, R. M. M.; Lemay, S. G.; Dekker, N. H.; Dekker, C. Direct Force Measurements on DNA in a Solid-State Nanopore. *Nat. Phys.* **2006**, *2*, 473–477.
97. Chang, H.; B. M. V.; Iqbal, S. M.; Andreadakis, G.; Kosari, F.; Vasmatzis, G. D. P.; Bashir, R. DNA Counterion Current and Saturation Examined by a Mems-Based Solid State Nanopore Sensor. *Biomed. Microdevices* **2006**, *8*, 263–269.
98. Fologea, D.; Uplinger, J.; Thomas, B.; McNabb, D. S.; Li, J. Slowing DNA Translocation in a Solid-State Nanopore. *Nano Lett.* **2005**, *5*, 1734–1737.
99. Sánchez-Quesada, J.; Saghatelian, A.; Cheley, S.; Bayley, H.; Ghadiri, M. R. Single DNA Rotaxanes of a Transmembrane Protein. *Angew. Chem., Int. Ed.* **2004**, *43*, 3063–3067.
100. Butler, T. Z.; Gundlach, J. H.; Troll, M. A. Determination of RNA Orientation During Translocation through a Biological Nanopore. *Biophys. J.* **2006**, *90*, 190–199.
101. Keyser, U. F.; van der Does, J.; Dekker, C.; Dekker, N. H. Optical Tweezers for Force Measurements on DNA in Nanopores. *Rev. Sci. Instrum.* **2006**, *77*, 105105.
102. Meller, A. Dynamics of Polynucleotide Transport through Nanometre-Scale Pores. *J. Phys.: Condens. Matter* **2003**, *15*, R581−R607.
103. Heng, J. B.; Aksimentiev, A.; Ho, C.; Marks, P.; Grinkova, Y. V.; Sligar, S.; Schulten, K.; Timp, G. The Electromechanics of DNA in a Synthetic Nanopore. *Biophys. J.* **2006**, *90*, 1098–1106.
104. Heng, J. B.; Aksimentiev, A.; Ho, C.; Marks, P.; Grinkova, Y. V.; Sligar, S.; Schulten, K.; Timp, G. Stretching DNA Using the Electric Field in a Synthetic Nanopore. *Nano Lett.* **2005**, *5*, 1883–1888.
105. Howorka, S.; Movileanu, L.; Braha, O.; Bayley, H. Kinetics of Duplex Formation for Individual DNA Strands within a Single Protein Nanopore. *Proc. Natl. Acad. Sci. U.S.A.* **2001**, *98*, 12996–13001.
106. Fologea, D.; Gershow, M.; Ledden, B.; McNabb, D. S.; Golovchenko, J. A.; Li, J. Detecting Single Stranded DNA with a Solid State Nanopore. *Nano Lett.* **2005**, *5*, 1905–1909.
107. Hornblower, B.; Coombs, A.; Whitaker, R. D.; Kolomeisky, A.; Picone, S. J.; Meller, A.; Akeson, M. Single-Molecule Analysis of DNA-Protein Complexes Using Nanopores. *Nat. Methods* **2007**, *4*, 315–317.
108. Winters-Hilt, S.; Vercoutere, W.; DeGuzman, V. S.; Deamer, D.; Akeson, M.; Haussler, D. Highly Accurate Classification of Watson-Crick Basepairs on Termini of Single DNA Molecules. *Biophys. J.* **2003**, *84*, 967–976.
109. Vercoutere, W.; Winters-Hilt, S.; Olsen, H.; Deamer, D.; Haussler, D.; Akeson, M. Rapid Discrimination among Individual DNA Hairpin Molecules at Single-Nucleotide Resolution Using an Ion Channel. *Nat. Biotechnol.* **2001**, *19*, 248–252.
110. Akeson, M.; Branton, D.; Kasianowicz, J. J.; Brandin, E.; Deamer, D. W. Microsecond Time-Scale Discrimination among Polycytidylic Acid, Polyadenylic Acid, and Polyuridylic Acid as Homopolymers or as Segments within Single Rna Molecules. *Biophys. J.* **1999**, *77*, 3227–3233.
111. Kubitschek, H. E. *Research (London)* **1960**, *13*, 128.
112. Carbonaro, A.; Sohn, L. L. A Resistive-Pulse Sensor Chip for Multianalyte Immunoassays. *Lab Chip* **2005**, *5*, 1155–1160.
113. Kullman, L.; Winterhalter, M.; Bezrukov, S. M. Transport of Maltodextrins through Maltoporin: A Single-Channel Study. *Biophys. J.* **2002**, *82*, 803–812.
114. Heins, E. A.; Siwy, Z. S.; Baker, L. A.; Martin, C. R. Detecting Single Porphyrin Molecules in a Conically Shaped Synthetic Nanopore. *Nano Lett.* **2005**, *5*, 1824–1829.
115. Danelon, C.; Lindemann, M.; Borin, C.; Fournier, D.; Winterhalter, M. Channel-Forming Membrane Proteins as Molecular Sensors. *IEEE Trans. Nanobiosci.* **2004**, *3*, 46–48.
116. Sutherland, T. C.; Long, Y. T.; Stefureac, R. I.; Bediako-Amoa, I.; Kraatz, H. B.; Lee, J. S. Structure of Peptides Investigated by Nanopore Analysis. *Nano Lett.* **2004**, *4*, 1273–1277.
117. Movileanu, L.; Howorka, S.; Braha, O.; Bayley, H. Detecting Protein Analytes That Modulate Transmembrane Movement of a Polymer Chain within a Single Protein Pore. *Nat. Biotechnol.* **2000**, *18*, 1091–1095.

118. Danelon, C.; Nestorovich, E. M.; Winterhalter, M.; Ceccarelli, M.; Bezrukov, S. M. Interaction of Zwitterionic Penicillins with the Ompf Channel Facilitates Their Translocation. *Biophys. J.* **2006**, *90*, 1617–1627.
119. Iqbal, S. M.; Akin, D.; Bashir, R. Solid-Stage Nanopore Channels with DNA Selectivity. *Nat. Nanotechnol.* **2007**, *2*, 243–248.
120. Tabard-Cossa, V.; Trivedi, D.; Wiggin, M.; Jetha, N. N.; Marziali, A. Noise Analysis and Reduction in Solid-State Nanopores. *Nanotechnology* **2007**, *18*, 305505.
121. Oukhaled, G.; Mathe, J.; Biance, A. L.; Bacri, L.; Betton, J. M.; Lairez, D.; Pelta, J.; Auvray, L. Unfolding of Proteins and Long Transient Conformations Detected by Single Nanopore Recording. *Phys. Rev. Lett.* **2007**, *98*, 158101.
122. Sexton, L. T.; Horne, L. P.; Martin, C. R. Developing Synthetic Conical Nanopores for Biosensing Applications. *Mol. Biosyst.* **2007**, *3*, 667–685.
123. Fologea, D.; Ledden, B.; McNabb, D. S.; Li, J. Electrical Characterization of Protein Molecules by a Solid-State Nanopore. *Appl. Phys. Lett.* **2007**, *91*, 053901.
124. Han, A.; Schürmann, G.; Mondin, G.; Bitterli, R. A.; Hegelbach, N. G.; de Rooij, N. F.; Staufer, U. Sensing Protein Molcules Using Nanofabricated Pores. *Appl. Phys. Lett.* **2006**, *88*, 093901.
125. Sexton, L. T.; Horne, L. P.; Sherrill, S. A.; Bishop, G. W.; Baker, L. A.; Martin, C. R. Resistive-Pulse Studies of Proteins and Protein/Antibody Complexes Using a Conical Nanotube Sensor. *J. Am. Chem. Soc.* **2007**, 13144–13152.
126. Colquhoun, D.; Sigworth, F. J. Fitting and Statistical Analysis of Single-Channel Records In *Single-Channel Recording*, 2nd ed.; Sakmann, B., Neher, E., Eds.; Plenum Press: New York, 1995; pp 483−587..
127. Kubitschek, H. E. Electronic Counting and Sizing of Bacteria. *Nature* **1958**, *182*, 234–235.
128. Liu, H.; Qian, S.; Bau, H. H. The Effect of Translocating Cylindrical Particles on the Ionic Current through a Nanopore. *Biophys. J.* **2007**, *92*, 1164–1177.
129. Levis, R. A.; Rae, J. L. Constructing a Patch Clamp Setup. *Methods Enzymol.* **1992**, *207*, 14–66.
130. Rae, J. L.; Levis, R. A. Glass Technology for Patch Clamp Electrodes. *Methods Enzymol.* **1992**, *207*, 66–92.
131. Sigworth, F. J. Electronic Design of the Patch Clamp In *Single-Channel Recording*, 2nd ed.; Sakmann, B., Neher, E., Eds.; Plenum Press: New York, 1995; pp 95−127..
132. Benndorf, K. Multiple Levels of Native Cardiac Na+ Channels at Elevated Temperature Measured with High-Bandwidth/Low-Noise Patch Clamp. *Pflügers Arch.* **1993**, *422*, 506–515.
133. Sigworth, F. J. Open Channel Noise I. Noise in Acetylcholine Receptor Currents Suggests Conformational Fluctuations. *Biophys. J.* **1985**, *47*, 709–720.
134. Verveen, A. A.; DeFelice, L. J. Membrane Noise. *Prog. Biophys. Mol. Biol.* **1974**, *28*, 189–265.
135. Wonderlin, W. F.; Finkel, A.; French, R. J. Optimizing Planar Lipid Bilayer Single-Channel Recordings for High Resolution with Rapid Voltage Steps. *Biophys. J.* **1990**, *58*, 289–297.
136. We would like to clarify the meaning of the term signal bandwidth. When measuring signals in the presence of noise, two distinct bandwidths should be considered: (Burdett, R. Signals in the Presence of Noise In *Handbook of Measuring System Design*; Sydenham, P. H., Thorn, R., Eds.; John Wiley & Sons Ltd: West Sussex, England, 2005; pp 827−830) the signal bandwidth and the noise bandwidth. Usually, the signal bandwidth is more important than the noise bandwidth since it determines the time resolution of the recordings. The noise bandwidth is only required for an accurate prediction of the root-mean square (rms) noise from theoretical equations and can be derived from the signal bandwidth as discussed in the section Theoretical Calculations of the rms Current Noise from Power Spectral Densities. The signal bandwidth of systems that attenuate all frequency content above a specific frequency (*e.g.*, a system that contains a low-pass filter) is typically defined as the frequency at which the signal (including its noise) has been attenuated by −3 dB (*i.e.*, the signal bandwidth is the frequency at which the power of the signal and noise output from the system has been attenuated by 50% compared to the power of the signal and noise input to the system). Since the frequency at which a low-pass filter attenuates the input signal by −3 dB is commonly defined as the cutoff frequency f_c of the filter (a definition we also used in this work), the terms signal bandwidth and cutoff frequency are often used interchangeably along with the terms −3 dB bandwidth and bandwidth. Here we will use the terms signal bandwidth and cutoff frequency synonymously in the text and f_c in the equations.
137. Raistrick, I. D.; Franceschetti, D. R.; Macdonald, J. R. Theory In *Impedance Spectroscopy*, 2nd ed.; Barsoukov, E., Macdonald, J. R., Eds.; John Wiley & Sons, Inc.: Hoboken, NJ, 2005; pp 27−128..
138. Hille, B. Elementary Properties of Pores In *Ion Channels of Excitable Membranes*, 3rd ed.; Sinauer Associates Inc: Sunderland, MA, 2001; pp 347−375..
139. Hall, J. E. Access Resistance of a Small Circular Pore. *J. Gen. Physiol.* **1975**, *66*, 531–532.
140. It is possible that the *distributed* resistance of the glass pores with conical geometry, represented in the Figure 2A by the total resistance of the cone R_c, in series with the *distributed* capacitance of the pores, represented in Figure 2A as the total capacitance of the cone C_c, could limit the bandwidth of this structure below the values estimated here. We do not think, however, that the bandwidth limitation of the pore would be significant compared to the bandwidth limitation of the recording electronics (headstage, amplifier, analog low-pass filter, and digitizer) of ∼52 kHz as discussed in the text.
141. The overall signal bandwidth of current recordings will thus not be limited by the bandwidth of the pores. It is important to realize that for the cylindrical pores used here, the resistance of the pore R_p did not affect the signal bandwidth since it was not in series with a significant capacitance. In the case of conical pores, the equivalent model circuit was complicated but based on the estimate performed here, we suggest that the bandwidth of the conical pores used in this work was at least 13 MHz. In general, as long as the pore structures do not generate a large resistance in series with a large capacitance (*i.e.*, as long as the product of $R \times C$ is smaller than $\sim 1 \times 10^{-6}$ Ohm F), the signal bandwidth will not be limited by the pore structure itself but rather by the recording electronics as discussed in the text.
142. While this relationship was derived for Gaussian filters, (see ref 126) it can also be used to approximate the signal bandwidth of measurements that employ low-pass Bessel filters since a low-pass Bessel filter with a large number of poles approximates the response of a low-pass Gaussian filter (see ref 126).
143. The third mode of this amplifier uses a feedback capacitor instead of a resistor to decrease the noise; however, due to the relatively large currents recorded in most pore-based sensing experiments (hundreds of picoamps to nanoamps), this capacitive feedback mode is often not practical because of the large number of resets required to discharge the feedback capacitor.
144. The manufacturer states that this signal bandwidth is lower than expected for a low-pass Bessel filter with a cutoff frequency of 100 kHz due to the signal bandwidth limitation of the electronics in the headstage of the amplifier (for a discussion of the electronic components used in a patch-clamp amplifier, see refs 129 and 131).
145. Shapovalov, G.; Lester, H. A. Gating Transitions in Bacterial Ion Channels Measured at 3 Ms Resolution. *J. Gen. Physiol.* **2004**, *124*, 151–161.
146. A more complicated situation would arise if the pore had a signal bandwidth of approximately 20−150 kHz (i.e., a signal bandwidth that would be close to that of the *HAFD*). In this instance, the overall signal bandwidth of the recording would be set by the filter combination of the

HAFD with the pore; a theoretical calculation of the overall signal bandwidth would be difficult to obtain. If the signal bandwidth of the pore would be less than approximately 20 kHz, then its signal bandwidth would then determine (*i.e.*, limit) the overall signal bandwidth of the current recordings (assuming the signal bandwidth of the *HAFD* would be ~52 kHz).

147. If the pore had signal bandwidth that was comparable to the signal bandwidth of the *HAFD* combination or the digital filter, then the exact overall signal bandwidth of the current recordings after digital filtering would be difficult to predict theoretically. In this case, the overall signal bandwidth would be smaller than the lowest signal bandwidth of the individual elements (pore, *HAFD*, digital filter); if a single element would have a signal bandwidth significantly lower than the other elements (by a factor of ~3), it would determine the overall signal bandwidth of the current recordings.
148. If only analog Bessel filters and digital Gaussian filters are used on the current trace, the overall signal bandwidth can be estimated using the following equation (see ref 126): $f_c = \sqrt{\{1/\{1/f_{c1}^2 + 1/f_{c2}^2\}\}}$, where f_{c1} is the signal bandwidth of the *HAFD* combination (here, ~52 kHz) and f_{c2} is the cutoff frequency of the digital filter.
149. Since we did not know the precise coefficients for a four pole low-pass Bessel filter or a low-pass Gaussian filter (as used in this work), we used the coefficients c_1, c_2, and c_3 as the best available approximation for all theoretical rms calculations performed in this report (the characteristics of a low-pass Bessel filter with an increasing number of poles approximates the response of a low-pass Gaussian filter, see reference 126).
150. MacAvoy, T. C.; Halaby, S. A. Substrates for Thin-Film Circuitry. *IEEE Trans. Component Parts* **1964**, *11*, 15–22.
151. http://www.goodfellow.com/csp/active/STATIC/A/Polyethylene_terephthalate.html.
152. We point out that the noise bandwidth of the headstage and amplifier, the dielectric noise of the substrate, and the thermal noise of the pore should even be calculated by using the signal bandwidth of the *HAFD* combination (or the *HAFD*-digital filter combination) if the pore has a signal bandwidth that is comparable to or less than the signal bandwidth of the *HAFD* combination. We make this recommendation because the ability of the pore to limit the signal bandwidth is due to the design of patch-clamp amplifiers and not due to the pore acting like a low-pass filter (see ref 131). Since the pore does not act like a low-pass filter, additional noise but not information is included in current traces when the signal bandwidth of the amplifier is greater than the signal bandwidth of the pore (see ref 11).
153. We also examined the accuracy of eq 4 if we would use $a = 1$ (no excess noise in the feedback resistor) as well as the values for C_a that we estimated from the specifications of the manufacturer and Sherman−Gold (see reference 11, $\beta = 0.1$, $C_a = 70$ pF; $\beta = 1$, $C_a = 25$ pF). In this case, the maximum error between the measured noise and the theoretical noise was smaller than 30% for both $\beta = 0.1$ and for $\beta = 1$ (not including the data points marked with an asterisk).
154. The overall signal bandwidth of the *HAFD*-digital filter combination was calculated by measuring the t_{10-90} risetime of a digitally filtered square wave that was coupled in capacitively. To compare theory with experimental results, we subtracted the experimentally measured quantization noise from the data (since the experimental quantization noise was a factor of 16 larger than its theoretical prediction).
155. To demonstrate rms noise values at highest achievable signal bandwidths (~52 kHz), we also included data points that were filtered only with the analog low-pass filter of the amplifier (*i.e.*, no digital filter was used); these data points are marked with an asterisk in Figure 5. We are uncertain what is causing the large amount of noise in the traces that were not filtered digitally. The "obvious" reason would be that the actual signal bandwidth was higher than what we expected; however, we determined all bandwidths in this graph experimentally from the t_{10-90} risetime. Another possibility is that the coefficients we used to calculate the noise bandwidth did not perfectly describe the filtering characteristics of the headstage-analog filter combination.
156. Although the headstage was properly shielded and grounded, we recorded a significant amount of noise in the capacitively generated square wave traces. This noise led to standard deviations (STD) that were ~5% of the measured, average 40 kHz signal bandwidth for pores fabricated in both glass and PET (the STD of the bandwidth of individual pores was up to 10% of the measured value). Equations 4 and 8 show that the predicted value of the noise is strongly dependent on the signal bandwidth (a large source of noise in the power spectral density of the headstage and amplifier is proportional to f^2 and the power spectral density of the dielectric noise is proportional to f). Thus, small inaccuracies in determining the signal bandwidth can have a noticeable effect on the predicted values of the current noise (especially at high signal-bandwidths).
157. Horowitz, P.; Hill, W. Precision Circuits and Low-Noise Techniques In *The Art of Electronics*, 2nd ed.; Cambridge University Press: New York, 1989; pp 391−470..
158. Sigworth, F. J.; Urry, D. W.; Prasad, K. U. Open Channel Noise III. High-Resolution Recordings Show Rapid Current Fluctuations in Gramicidin A and Four Chemical Analogues. *Biophys. J.* **1987**, *52*, 1055–1064.
159. Heinemann, S. H.; Sigworth, F. J. Open Channel Noise V. Fluctuating Barriers to Ion Entry in Gramicidin A Channels. *Biophys. J.* **1990**, *57*, 499–514.
160. Lauger, P. Shot Noise in Ion Channels. *Biochim. Biophys. Acta* **1975**, *413*, 1–10.
161. Mak, D. O.; Webb, W. W. Molecular Dynamics of Alamethicin Transmembrane Channels from Open-Channel Current Noise Analysis. *Biophys. J.* **1995**, *69*, 2337–2349.
162. Robinson, F. N. H., *Noise and Fluctuations in Electronic Devices and Circuits*; Oxford University Press: London, England, 1974.
163. Nanopores under certain conditions may contain a potential barrier and can be strongly rectifying (see references 40, 50– 52, 66, and 67); these pores may therefore require a shot noise term to predict the noise accurately.
164. Many of the power spectra examined showed trends similar to Figure 8. In some power spectra, however, the noise power had a sigmoidal shape (*i.e.*, initially the noise power would grow in a linear fashion with decreasing frequency but would eventually reach a steady value at the lowest frequencies).
165. Ke, K.; Hasselbrink, E. F.; Hunt, A. J. Rapidly Prototyped Three-Dimensional Nanofludic Channel Networks in Glass Substrates. *Anal. Chem.* **2005**, *77*, 5083–5088.
166. Joglekar, A. P.; Liu, H.; Meyhöfer, E.; Mourou, G.; Hunt, A. J. Optics at Critical Intensity: Applications to Nanomorphing. *Proc. Natl. Acad. Sci. U.S.A.* **2004**, *101*, 5856–5861.
167. Joglekar, A. P.; Liu, H.; Spooner, G. J.; Meyhöfer, E.; Mourou, G.; Hunt, A. J. A Study of the Deterministic Character of Optical Damage by Femtosecond Laser Pulses and Applications to Nanomachining. *Appl. Phys. B: Lasers Opt.* **2003**, *77*, 25–30.
168. Ke, K.; Hasselbrink, E.; Hunt, A. J. Nanofabrication with Ultrafast Lasers at Critical Intensity. *Proc. Int. Soc. Opt. Eng.* **2005**, *5714*, 53–62.